

1 Temperate rainforests near the South Pole during peak
2 Cretaceous warmth

3

4 Klages, J.P.^{1*}, Salzmann, U.², Bickert, T.³, Hillenbrand, C.-D.⁴, Gohl, K.¹, Kuhn, G.¹,
5 Bohaty, S.⁵, Titschack, J.^{3,6}, Müller, J.^{1,7}, Frederichs, T.⁷, Bauersachs, T.⁸, Ehrmann,
6 W.⁹, van de Flierdt, T.¹⁰, Simões Pereira, P.¹⁰⁺, Larter, R.D.⁴, Lohmann, G.^{1,3,11},
7 Niezgodzki, I.^{1,12}, Uenzelmann-Neben, G.¹, Zundel, M.⁷, Spiegel, C.⁷, Mark, C.¹³⁺⁺,
8 Chew, D.¹³, Francis, J.E.⁴, Nehrke, G.¹, Schwarz, F.², Smith, J.A.⁴, Freudenthal, T.³,
9 Esper, O.¹, Pälike, H.³, Ronge, T.¹, Dziadek, R.¹, and the Science Team of
10 Expedition PS104[‡]

11

12 ¹ Alfred-Wegener-Institut Helmholtz-Zentrum für Polar- und Meeresforschung, Bremerhaven, Germany

13 ² Northumbria University, Department of Geography and Environmental Sciences, Newcastle upon Tyne, United
14 Kingdom

15 ³ MARUM – Center for Marine Environmental Sciences, Bremen, Germany

16 ⁴ British Antarctic Survey, Cambridge, United Kingdom

17 ⁵ School of Ocean and Earth Science, University of Southampton, Southampton, United Kingdom

18 ⁶ Senckenberg am Meer (SAM), Marine Research Department, Wilhelmshaven, Germany

19 ⁷ University of Bremen, Faculty of Geosciences, Bremen, Germany

20 ⁸ Christian-Albrechts-University, Institute of Geoscience, Kiel, Germany

21 ⁹ University of Leipzig, Institute for Geophysics and Geology, Leipzig, Germany

22 ¹⁰ Imperial College London, Department of Earth Science & Engineering, London, United Kingdom

23 ¹¹ University of Bremen, Environmental Physics, Bremen, Germany

24 ¹² ING PAN – Institute of Geological Sciences, Polish Academy of Sciences, Biogeosystem Modelling Laboratory,
25 Kraków, Poland

26 ¹³ Department of Geology, Trinity College Dublin, Dublin, Ireland

27 ⁺ now at: University of Gothenburg, Department of Marine Sciences, Gothenburg, Sweden

28 ⁺⁺ now at: School of Earth Sciences, University College Dublin, Dublin, Ireland

29 [‡] A full list of authors and their affiliations appears at the end of the paper

30 ^{*} Corresponding author: Johann.Klages@awi.de

31 **The mid-Cretaceous was one of the warmest intervals of the past 140 million years**
32 **(Myr)^{1–5} driven by atmospheric CO₂ levels around 1000 ppmv⁶. In the near absence of**
33 **proximal geological records from south of the Antarctic Circle, it remains disputed**
34 **whether polar ice could exist under such environmental conditions. Here we present**
35 **results from a unique sedimentary sequence recovered from the West Antarctic shelf.**
36 **This by far southernmost Cretaceous record contains an intact ~3 m-long network of**
37 ***in-situ* fossil roots. The roots are embedded in a mudstone matrix bearing diverse**
38 **pollen and spores, indicative of a temperate lowland rainforest environment at a**
39 **palaeolatitude of ~82°S during the Turonian–Santonian (92–83 Myr). A climate model**
40 **simulation shows that the reconstructed temperate climate at this high latitude**
41 **requires a combination of both atmospheric CO₂ contents of 1120–1680 ppmv and a**
42 **vegetated land surface without major Antarctic glaciation, highlighting the important**
43 **cooling effect exerted by ice albedo in high-CO₂ climate worlds.**

44
45 The Cretaceous Period (144–66 Myr) hosted some of the warmest intervals in Earth's
46 history^{1–3}, particularly during its Turonian to Santonian stages (93.9–83.6 Myr)^{4,5}. At that time,
47 atmospheric carbon dioxide (CO₂) concentrations were reconstructed to be around 1000
48 ppmv⁶, and average annual low latitude sea surface temperatures probably reached ~35°C⁴,
49 with only a minor bi-hemispheric temperature gradient extending poleward from palaeo-
50 latitudes between 50–60°N (refs. 7–9). Only small to medium-sized ice sheets may have
51 existed^{10,11} and global sea level was up to 170 m higher than at present^{11,12}.

52 Records documenting the Antarctic terrestrial environment during mid-Cretaceous warmth
53 are sparse^{5,13–17} and particularly rare south of the palaeo-Antarctic Circle^{13,14}. Such records,
54 however, are critical to constrain state-of-the-art Late Cretaceous climate models⁵ for
55 predicting the magnitude of atmospheric CO₂ concentrations¹⁸ and their effectiveness in
56 inhibiting the build-up of major ice sheets¹⁹.

57 Here we reconstruct mid-Cretaceous terrestrial environmental conditions in West Antarctica
58 by combining micro- and macropalaeontological, sedimentological, inorganic and organic
59 geochemical, mineralogical, and palaeomagnetic data as well as X-ray computed
60 tomography (CT) imagery obtained from drill cores recovered from a site within the Pine
61 Island cross-shelf trough in the Amundsen Sea Embayment (ASE), West Antarctica (Fig. 1a).
62 Site PS104_20-2 (73.57°S, 107.09°W; 946 m water depth) was drilled during RV *Polarstern*
63 expedition PS104 in 2017 (ref. 22). The Pine Island Trough extends from the modern fronts
64 of Pine Island and Thwaites glaciers, and was eroded into the ASE shelf during repeated
65 advances of a West Antarctic Ice Sheet (WAIS) palaeo-ice stream throughout Miocene–
66 Pleistocene epochs^{23–25}. On the inner–middle continental shelf, glacial erosion combined with
67 tectonic uplift²⁴ exposed seaward-dipping sedimentary strata of postulated Cretaceous to
68 Miocene age near the seafloor²⁶ (Fig. 1b). Widespread till cover on the shelf previously
69 prevented sampling of these strata using conventional coring techniques²⁶. Deployment of
70 the remotely operated seafloor drill rig *MARUM-MeBo70* (ref. 27) enabled drilling to 30.7
71 metres below sea floor (mbsf) into the seabed and recover the dipping strata²² (Figs. 1, 2).

72

73 **Lithology and stratigraphy**

74 Beneath a few meters of glacimarine and reworked glacial sediments, *MARUM-MeBo70*
75 penetrated occasionally stratified but microfossil-barren ca. 17 to 24 m-thick quartzitic
76 sandstone with uranium/lead (U/Pb) dates on apatite and zircon grains (see Methods)
77 constraining its maximum depositional age to ~40 Myr in the late Eocene (Extended Data
78 Fig. 1). Cores 9R and 10R recovered strata from 26.3 mbsf to the base of the hole. At ca.
79 26.8 mbsf, a prominent 5 cm thin layer of indurated lignite fragments separates the overlying
80 sandstone unit from a ≥3 m-thick palynomorph-rich, laminated to stratified carbonaceous
81 mudstone below. This mudstone contains an intact and continuous network of fossil plant
82 roots that reaches down to at least ~30 mbsf (Fig. 2; Supplementary Video 1).

83 Based on New Zealand's biostratigraphic ranges²⁸, the presence of the pollen taxon
84 *Phyllocladites mawsonii* (Nearest Living Relative (NLR): *Lagarostrobos*, Huon Pine) and the

85 absence of both *Nothofagidites* (NLR: *Nothofagus*, Southern Beech) and *Forcipites*
86 *sabulosus* within the carbonaceous mudstone indicate its deposition during the mid-
87 Cretaceous (Turonian–Santonian; ~92–83 Myr, PM1a-subzone) (Extended Data Fig. 2;
88 Extended Data Tables 1, 2). Abundant pollen of conifer trees (e.g. *Podocarpidites*,
89 *Trichotomosulcites*), tree ferns (*Cyathidites*), and the presence of accessory taxa such as
90 *Ruffordiaspora ludbrookiae* and *Tricolpites* spp. in our assemblage resemble the uppermost
91 strata of the Turonian–Santonian Tupuangi Formation on Pitt Island, New Zealand, dated to
92 92-89 Myr^{29,30} (Extended Data Table 3). However, the regular occurrence of pollen of the
93 family Proteaceae, including *Beauprea*-type pollen (e.g. *Peninsulapollis gillii*, *Beaupreaidites*),
94 which are absent from the Tupuangi Formation, suggest the ASE core to be slightly younger
95 than 89 Myr. Recent molecular phylogenetic reconstructions indicate an early Antarctic-
96 Southeastern Australian origin of *Beauprea* (~88 Myr ago), while the oldest palynological
97 record of these angiosperm fossils on Antarctica and Australia date back to 81.4 Myr and
98 83.8 Myr, respectively³¹.
99 These biostratigraphic age estimates are consistent with palaeomagnetic data obtained from
100 discrete sediment samples showing normal polarity, expected for deposition during the
101 ‘Cretaceous Normal Polarity Superchron’ (C34n; 121–83 Myr; ref. 32) (see Methods). The
102 layer of indurated lignite and the underlying carbonaceous mudstone show very similar
103 pollen assemblages, which indicate a similar age and palaeoenvironment for both units (Fig.
104 2; Extended Data Fig. 2).

105

106 **Turonian–Santonian position of the record**

107 In order to assess the palaeoclimatic significance of this record, we determined the
108 palaeogeographical position of site PS104_20-2 at 90 Myr. Today, the site is located near
109 the Pacific continental margin of West Antarctica about 250 km away from the modern
110 boundary between continental and oceanic crust³⁴ (Fig. 1). At the time of sediment deposition
111 between 93 and 83 Myr, the continent of Zealandia started to rift and separate from West
112 Antarctica^{33,34}. We applied a relative plate reconstruction between Zealandia and West

113 Antarctica for the middle Cretaceous using the *GPlates* plate reconstruction tool³⁵ with up-to-
114 date rotation parameters of the South Pacific realm³³. This resulted in a 736-km great-circle
115 distance (265 km North-South distance) between the drill site and the hitherto southernmost
116 mid-Cretaceous terrestrial palaeoenvironmental record on Pitt Island on Chatham Rise, New
117 Zealand¹⁴. The close fit reconstruction at 90 Myr indicates a wide rift zone between
118 Zealandia and West Antarctica, just before initiation of the continental breakup^{26,33}. In a
119 previous study³⁶, a 100-Myr mean palaeomagnetic pole position of 75.7°S and 135.9°W with
120 a 95% confidence radius of 3.8° for Marie Byrd Land was determined from 19 rock sample
121 sites. By accounting for the great-circle distance of 7.84° to our drill site and rotating points
122 on the East Antarctic polar wander path³⁶ into the Marie Byrd Land reference frame, we
123 derive a core site palaeolatitude of 81.9°S at 90 Myr. Its uncertainty is estimated to be not
124 larger than the maximum 95% confidence radius of 5.9° of the respective part of the polar
125 wander path³⁶.

126

127 **Palaeoenvironment**

128 The indurated lignite layer as well as the laminated to stratified carbonaceous mudstone
129 comprising the fossil plant roots in cores 10R and lower 9R at site PS104_20-2 contain a
130 highly diverse and entirely terrestrial palynomorph assemblage of more than 62 pollen and
131 spore taxa (Fig. 2; Extended Data Figs. 2, 3; Extended Data Table 3). The absence of
132 palynomorphs with different stratigraphic ranges or varying thermal maturity suggests that
133 this purely terrestrial microfossil assemblage has not been reworked. The assemblage is
134 dominated by pollen of the conifer tree families Podocarpaceae and Araucariaceae with
135 abundant ferns, including the tree ferns *Cyathea*, documenting the initial stages of an Austral
136 temperate rainforest (Fig. 2; Extended Data Fig. 2; Extended Data Table 2). The presence of
137 the heterocyst glycolipids HG₃₀ triol and keto-diol (Extended Data Fig. 4; see Methods) also
138 indicates that benthic cyanobacterial mats colonized fresh water bodies within this temperate
139 rainforest, providing additional evidence for the development of a highly complex ecosystem
140 in the ASE during the Turonian–Santonian. In combination with published palaeo-

141 topographic and palaeo-tectonic information^{24,26,33}, the different taxa and their bioclimatic
142 significance (see Methods) were combined and visualized to create Fig. 4. Members of the
143 Proteaceae family presumably formed a flowering shrub understorey in the tall Late
144 Cretaceous conifer rainforest of the ASE depicted in Fig. 4. The lignite layer is rich in spores
145 of *Stereisporites antiquasporites* (NLR: Bryophyte, *Sphagnum*), which further suggest the
146 temporary existence of a peat swamp in the diverse temperate lowland rainforest. This
147 coincides with increasing *Peninsulapollis* pollen indicating increasing humidity³⁷ towards the
148 record's top. Thin sections were carefully prepared from resin-impregnated core samples
149 selected from cores 9R and 10R (see Methods) to characterize the fossil roots. Although cell
150 structures were not sufficiently preserved for identification of the plant that grew the roots, the
151 presence of parenchyma cells within the long and continuous roots likely identifies the
152 network as vascular plant remains and thus confirms active plant growth at our site
153 (Extended Data Fig. 5b–e). Further, the alignment of organic and clastic material within the
154 laminated to stratified mudstone matrix (Extended Data Fig. 5a) suggests synchronous
155 deposition of clastic particles and organic fragments.

156 Our environmental reconstruction is further supported by geochemical and biomarker data. In
157 the mudstone between 29.80 and 27.03 mbsf and the indurated lignite interval (26.83–26.77
158 mbsf), absent to very low halite and carbonate contents in the bulk sediment fraction
159 combined with low total organic carbon/total nitrogen (TOC/TN) ratios and low ratios of
160 higher land-plant-derived long-chain *n*-alkanes versus aquatic-sourced short-chain *n*-alkanes
161 (TAR) point to swampy aquatic freshwater conditions (Fig. 2). This interpretation is supported
162 by the identification of cells closely resembling aerenchyma (Extended Data Fig. 5d) usually
163 being responsible for inter-cellular gas exchange under (semi-) permanent subaquatic
164 growing conditions³⁸. In mudstone samples taken from the core segment containing a
165 particularly dense root network (27.03–26.83 mbsf), pollen and biomarkers indicate the
166 establishment of terrestrial forest-type vegetation, whilst elevated pristane/*n*-C₁₇ and
167 pristane/phytane ratios point to high abundance of terrigenous plant material (Extended Data
168 Fig. 6; cf. refs. 39, 40), which is in line with the pollen-based interpretation of a terrestrial

169 rainforest environment. TOC/TN ratios >20 (Fig. 2) are consistent with this interpretation and
170 indicate a primarily land plant source of organic matter⁴¹ within this mudstone sequence.

171 The clay mineral assemblage in cores 9R and 10R is dominated by kaolinite (67–72%) and
172 smectite (26–29%), both indicating chemical weathering activity under humid and (sub-)
173 tropical climate conditions⁴². However, as this is not corroborated by our reconstructed
174 climatic setting, we attribute kaolinite formation in the mudstone predominantly to the
175 establishment of repeated swampy conditions, in which organic acids altered silicate
176 minerals to kaolinite (= ‘Moorverwitterung’)⁴³.

177 The lithological succession in cores 9R and 10R resemble the uppermost strata of the
178 Turonian–Santonian Tupuangi Formation on Pitt Island, New Zealand²⁹. The Pitt Island strata
179 are characterized by interbedded carbonaceous siltstone, quartzo-feldspathic sandstone and
180 lignite and/or peat layers. Similar to the sediment sequence described for the ASE, the
181 Tupuangi Formation records a terrestrial, densely vegetated, and partly swampy fluviodeltaic
182 environment¹⁴. Some 90 million years ago, the Tupuangi Formation was located in one of the
183 rift basins developing before Zealandia separated from West Antarctica^{26,33}, ~736 km away
184 from Site PS104_20-2 (Fig. 1). A diverse conifer forest surrounded by extensive river
185 systems^{44,45} appears to have covered both the Zealandian¹⁴ and the West Antarctic
186 conjugate continental margin during this early break-up phase.

187 The sharp lithological change from the fossil root-bearing mudstone with the thin layer of
188 indurated lignite on top into the sandstone at 26.77 mbsf is marked by increased iron
189 carbonate and halite contents and decreased TOC/TN and TAR ratios within the sandstone
190 (Fig. 2), suggesting an estuarine and coastal environment. The U/Pb dates of max. ~40 Myr
191 obtained from the sandstone (see Extended Data Fig. 1), which is coarse-grained at its base,
192 indicate a significant hiatus between the mudstone (including the lignite) and the sandstone.
193 Such a hiatus is consistent with neodymium (Nd) and strontium (Sr) isotope data, reflecting
194 both a change in sediment provenance and a decrease in weathering intensity between the
195 two lithologies (Fig. 2; see Methods). The time window of the hiatus coincides with slow
196 erosion rates of a tectonically quiescent passive margin^{24,46}, whereas Eocene/Oligocene

197 tectonic activity of the West Antarctic Rift System might have triggered renewed
198 sedimentation of dominantly clastic material^{46,47}.

199

200 **Palaeoclimate**

201 Multi-proxy evidence from our mid-Cretaceous sedimentary record reveals an environment at
202 a palaeolatitude of ~82°S on the Antarctic continental margin that was characterised by a
203 regional temperate climate warm enough to maintain a diverse temperate rainforest (Fig. 4)
204 only ~900 km away from the palaeo-South Pole. Our palynomorph-based climate
205 reconstruction based on the approach outlined in ref. 48 indicates mean annual temperatures
206 of 13°C with precipitation around 1,120 mm/year. The temperature of the warmest summer
207 month was around 18.5°C on average. Previous quantitative climate analyses from Antarctic
208 records ~2,500 km further north resulted in late Coniacian–early Santonian mean annual
209 temperatures of 15–21°C^{49,50}, suggesting a shallow gradient to our site. NLR-based
210 estimates of Late Cretaceous climate generally agree well with other temperature proxies⁴⁹.
211 However, the approach assumes similarity of climate requirements for fossil taxa and their
212 NLRs. As with increasing age the phylogenetic relationships of a fossil taxon become more
213 disparate, the assumption becomes less robust. We therefore applied an independent
214 geochemical palaeothermometer based on heterocyst glycolipid distribution (HTI₃₀)⁵¹, which
215 corroborated our bioclimatic reconstructions by indicating austral summer lake or river-
216 surface temperatures of ~20°C for the swampy rainforest (Extended Data Fig. 4; see
217 Methods). Our record contains the hitherto southernmost evidence of Cretaceous terrestrial
218 environmental conditions and reveals a mid-Cretaceous ‘greenhouse climate’ that was
219 capable of maintaining temperate conditions much further south than previously
220 documented¹⁴.

221

222 **Palaeoclimate modelling**

223 In light of extremely limited mid-Cretaceous CO₂ proxy data⁶ and widely scattered existing
224 data estimates⁵ and in order to identify some of the pivotal driving mechanism of high-latitude

225 mid-Cretaceous environmental conditions reconstructed for our new record, we ran the
226 global climate model COSMOS⁵ in a coupled atmosphere–ocean configuration with fixed
227 vegetation. We did so under present (Fig. 3a-c) and mid-Cretaceous configurations at 90 Myr
228 (Fig. 3d-g) for 1x, 2x, 4x and 6x pre-industrial CO₂ levels of 280 ppm (280, 560, 1120 and
229 1680 ppmv, respectively; see Methods). Although the model predicts a mid-Cretaceous
230 climate in West Antarctica that is already warmer under pre-industrial CO₂ levels of 280 ppm
231 (Fig. 3d), summer surface air and water temperatures of ~20°C at ~82°S can only be
232 reproduced by forcing the climate with very high atmospheric CO₂ levels between 1120 and
233 1680 ppmv (Fig. 3f, g). Our reconstructed mean annual temperature of 13°C, however, still
234 remains significantly underestimated by the model (Fig. 3g).

235 We conclude that a temperate climate at such a high latitude with more than four months of
236 complete polar night darkness requires a combination of both strongly elevated atmospheric
237 CO₂ concentrations and dense surface vegetation that generates a low planetary albedo with
238 an associated high radiant energy absorption and pronounced seasonality. This largely
239 excludes the existence¹⁰ of any substantial ice-sheet and sea-ice cover in and around
240 Antarctica during the Turonian to Santonian stages of the Late Cretaceous epoch, likely
241 additionally favoured by palaeo-geographic variations⁵². Conversely, the present Antarctic
242 Ice Sheet and its associated climate feedbacks, such as the ice albedo, provide a stabilizing
243 cooling effect in a future high-CO₂ world (Fig. 3a-c).

244 To further elaborate on the significance of additional forcing mechanisms, to discover the
245 interdependency of surface vegetation and temperature sensitivity in more detail, and to
246 explore the drivers of the late Cretaceous latitudinal gradient paradox visible in Fig. 3, future
247 work will aim at running the model with various types of vegetation cover coupled with other
248 drivers such as palaeo-geography⁵² or changes in cloudiness⁵³.

249 Our findings highlight the importance of including land–ice changes into long-term climate
250 simulations in order to accurately estimate climate sensitivity on these extended time
251 scales⁵⁴. We provide new key data for constraining the response of polar terrestrial
252 ecosystems to very high atmospheric CO₂ concentrations and for assessing the significance

253 of Antarctic ice sheet presence under high-CO₂ scenarios – essential for modelling both past
254 and future climate change⁵⁵.

255

- 256 1. Forster, A., Schouten, S., Baas, M. & Sinninghe Damsté, J. S. Mid-Cretaceous
257 (Albian–Santonian) sea surface temperature record of the tropical Atlantic Ocean.
258 *Geology* **35**, 919–922 (2007a).
- 259 2. Forster, A. et al. Tropical warming and intermittent cooling during the
260 Cenomanian/Turonian Oceanic Anoxic Event (OAE 2): Sea surface temperature
261 records from the equatorial Atlantic. *Paleoceanography* **22**, PA1219 (2007b).
- 262 3. Tarduno, J. A. et al. Evidence for Extreme Climatic Warmth from Late Cretaceous
263 Arctic Vertebrates. *Science* **282**, 2241–2243 (1998).
- 264 4. O'Brien, C. L. et al. Cretaceous sea-surface temperature evolution: Constraints from
265 TEX₈₆ and planktonic foraminiferal oxygen isotopes. *Earth-Sci. Rev.* **172**, 224–247
266 (2017).
- 267 5. Niezgodzki, I. et al. Late Cretaceous climate simulations with different CO₂ levels and
268 subarctic gateway configurations: A model-data comparison. *Paleoceanography* **32**,
269 980–998 (2017).
- 270 6. Foster, G. L., Royer, D. L. & Lunt, D. J. Future climate forcing potentially without
271 precedent in the last 420 million years. *Nat. Comm.* **8**, doi:10.1038/ncomms14845,
272 (2017).
- 273 7. O'Connor, L. K. et al. Late Cretaceous Temperature Evolution of the Southern High
274 Latitudes: A TEX₈₆ Perspective. *Paleoceanography and Paleoclimatology* **34**,
275 doi:10.1029/2018PA003546 (2019).
- 276 8. Jenkyns, H. C., Forster, A., Schouten, S. & Sinninghe Damsté, S. High temperatures
277 in the Late Cretaceous Arctic Ocean. *Nature* **432**, 888–892 (2004).
- 278 9. Ditchfield, P. W., Marshall, J. D. & Pirrie, D. High latitude palaeotemperature
279 variation: New data from the Tithonian to Eocene of James Ross Island, Antarctica.
280 *Palaeogeogr. Palaeoclimatol. Palaeoecol.* **107**, 79–101 (1994).

- 281 10. Bornemann, A. et al. Isotopic Evidence for Glaciation During the Cretaceous
282 Supergreenhouse. *Science* **319**, 189–192 (2008).
- 283 11. Müller, R. D. et al. Long-Term Sea-Level Fluctuations Driven by Ocean Basin
284 Dynamics. *Science* **319**, 1357–1362 (2008).
- 285 12. Miller, K. G. et al. The Phanerozoic Record of Global Sea-Level Change. *Science*
286 **310**, 1293–1298 (2005).
- 287 13. Mcphail, M. K., Truswell, E. M. Palynology of Site 1166, Prydz Bay, East Antarctica.
288 *In: Cooper, A. K., O'Brien, P. E. and Richter, C. (eds.) Proceedings of the Ocean*
289 *Drilling Program, Scientific Results, College Station, TX (Ocean Drilling Program)*
290 **188**, 1–43 (2004).
- 291 14. Mays, C., Steinhorsdottir, M. & Stilwell, J. D. Climatic implications of *Ginkgoites*
292 *waarrensis* Douglas emend. from the south polar Tupuangi flora, Late Cretaceous
293 (Cenomanian), Chatham Islands. *Palaeogeogr. Palaeoclimatol. Palaeoecol.* **438**,
294 308–326 (2015).
- 295 15. Pujana, R. R., Raffi, M. E. & Olivero, E. B. Conifer fossil woods from the Santa Marta
296 Formation (Upper Cretaceous), Brandy Bay, James Ross Island, Antarctica.
297 *Cretaceous Research* **77**, 28–38 (2017).
- 298 16. Manfroi, J. et al. The first report of a Campanian palaeo-wildfire in the West Antarctic
299 Peninsula. *Palaeogeogr. Palaeoclimatol. Palaeoecol.* **418**, 12–18 (2015).
- 300 17. Falcon-Lang, H. J., Cantrill, D. J. & Nichols, G. J. Biodiversity and terrestrial ecology
301 of a mid-Cretaceous, high-latitude floodplain, Alexander Island, Antarctica. *J. Geol.*
302 *Soc. Lond.* **158**, 709–724 (2001).
- 303 18. Wang, Y., Huang, C., Sun, B., Quan, C., Wu, J. & Lin, Z. Paleo-CO₂ variation trends
304 and the Cretaceous greenhouse climate. *Earth-Sci. Rev.* **129**, 136–147 (2014).
- 305 19. Huber, B. T., MacLeod, K. G., Watkins, D. K. & Coffin, M. F. The rise and fall of the
306 Cretaceous Hot Greenhouse climate. *Glob. Planet. Change* **167**, 1–23 (2018).
- 307 20. Arndt, J. E. et al. A new bathymetric compilation covering circum-Antarctic waters.
308 *Geophys. Res. Lett.* **40**, 1–7 (2013).

- 309 21. Fretwell, P. et al. Bedmap2: improved ice bed, surface and thickness datasets for
310 Antarctica. *The Cryosphere* **7**, 375–393 (2013).
- 311 22. Gohl, K. et al. MeBo70 seabed drilling on a polar continental shelf: operational report
312 and lessons from drilling in the Amundsen Sea Embayment of West Antarctica.
313 *Geochem. Geophys. Geosys.* **18**, 4235–4250 (2017).
- 314 23. Lowe, A. L. & Anderson, J. B. Reconstruction of the West Antarctic ice sheet in Pine
315 Island Bay during the Last Glacial Maximum and its subsequent retreat history. *Quat.*
316 *Sci. Rev.* **21**, 1879–1897 (2002).
- 317 24. Spiegel, C. et al. Tectonomorphic evolution of Marie Byrd Land – Implications for
318 Cenozoic rifting activity and onset of West Antarctic glaciation. *Glob. Planet. Change*
319 **145**, 98–115 (2016).
- 320 25. Larter, R. D. et al. Reconstruction of changes in the Amundsen Sea and
321 Bellingshausen Sea sector of the West Antarctic Ice Sheet since the Last Glacial
322 Maximum. *Quat. Sci. Rev.* **100**, 55–86 (2014).
- 323 26. Gohl, K. et al. Seismic stratigraphic record of the Amundsen Sea Embayment shelf
324 from pre-glacial to recent times: Evidence for a dynamic West Antarctic ice sheet.
325 *Mar. Geol.* **344**, 115–131 (2013).
- 326 27. Freudenthal, T. & Wefer, G. Drilling cores on the sea floor with the remote-controlled
327 sea floor drilling rig MeBo. *Geoscientific Instrumentation, Methods and Data Systems*
328 **2**, 329–337 (2013).
- 329 28. Crampton, J. S. et al. Cretaceous (Taitai, Clarence, Raukumara and Mata Series). In:
330 Cooper, R.A. (Ed.), The New Zealand Geological Timescale. R. A. Cooper. Lower
331 Hutt, Institute of Geological and Nuclear Sciences Limited. *Geological & Nuclear*
332 *Sciences Monograph* **22**, 102–122 (2004).
- 333 29. Mays, C. & Stilwell, J. D. Pollen and spore biostratigraphy of the mid-Cretaceous
334 Tupurangi Formation, Chatham Islands, New Zealand. *Rev. Palaeobot. Palynol.* **192**,
335 79–102 (2013).

- 336 30. Mildenhall, D. C. Palynological reconnaissance of Early Cretaceous to Holocene
337 sediments, Chatham Islands, New Zealand. *Institute of Geological & Nuclear*
338 *Sciences monograph 7* in *New Zealand Geological Survey paleontological bulletin 67*,
339 204 p. (1994).
- 340 31. He, T., Lamont, B. B. & Fogliani, B. Pre-Gondwanan-breakup origin of *Beauprea*
341 (Proteaceae) explains its historical presence in New Caledonia and New Zealand,
342 *Science Advances 2*, E1501648 (2016).
- 343 32. Gee, J. & Kent, D. Source of Oceanic Magnetic Anomalies and the Geomagnetic
344 Polarity Timescale. In: *Treatise on Geophysics*, vol. 5., Geomagnetism, Chapter 5.12,
345 Elsevier, Editor: M. Kono, pp. 455-507, doi:10.1016/B978-044452748-6/00097-3
346 (2007).
- 347 33. Wobbe, F., Gohl, K., Chambord, A. & Sutherland, R. Structure and breakup history of
348 the rifted margin of West Antarctica in relation to Cretaceous separation from
349 Zealandia and Bellingshausen plate motion. *Geochem. Geophys. Geosys. 13*, 1–19
350 (2012).
- 351 34. Mortimer, N. et al. Late Cretaceous oceanic plate reorganization and the breakup of
352 Zealandia and Gondwana. *Gondwana Res. 65*, 31–42 (2019).
- 353 35. Müller, R. D. et al. GPlates: Building a Virtual Earth Through Deep Time. *Geochem.*
354 *Geophys. Geosys. 19*, 2243–2261 (2018).
- 355 36. DiVenere, V. J., Kent, D. V. & Dalziel, I. W. D. Mid-Cretaceous paleomagnetic results
356 from Marie Byrd Land, West Antarctica: A test of post-100 Ma relative motion between
357 East and West Antarctica, *Journal of Geophysical Research 99*, B8, 15115–15139
358 (1994).
- 359 37. Pocknall, D. T. & Crosbie, Y. M. Pollen morphology of *Beauprea* (Proteaceae): Modern
360 and fossil. *Rev Palaeobot and Palynol 53*, 305–327 (1988).
- 361 38. Jackson, M. B. & Armstrong, W. Formation of Aerenchyma and the Processes of
362 Plant Ventilation in Relation to Soil Flooding and Submergence. *Plant Biol 1*, 274–287
363 (1999).

- 364 39. Lijmbach, G. W. M. On the origin of petroleum. *Proceedings of the 9th world*
365 *petroleum congress* **2**, 357–369 (1975).
- 366 40. Peters, K. E., Walters, C. C. & Moldowan, J. M. The Biomarker Guide. *Cambridge*
367 *University Press*, 1155 p. (2004).
- 368 41. Meyers, P. A. Applications of organic geochemistry to paleolimnological
369 reconstructions: a summary of examples from the Laurentian Great Lakes. *Org.*
370 *Geochem.* **34**, 261–289 (2003).
- 371 42. Robert, C. & Kennett, J. P. Antarctic subtropical humid episode at the Paleocene–
372 Eocene boundary: Clay-mineral evidence. *Geology* **22**, 211–214 (1994).
- 373 43. Huang, W. H. & Keller, W. D. Dissolution of rock-forming silicate minerals in organic
374 acids: Simulated first-stage weathering of fresh mineral surfaces. *The American*
375 *Mineralogist* **55**, 2076–2094 (1970).
- 376 44. Sugden, D. E. & Jamieson, S. S. R. The pre-glacial landscape of Antarctica. *Scottish*
377 *Geographical Journal* **134**, 203–223 (2018).
- 378 45. Uenzelmann-Neben, G. & Gohl, K. Early glaciation already during the Early Miocene
379 in the Amundsen Sea, Southern Pacific: Indications from the distribution of
380 sedimentary sequences. *Glob. Planet. Change* **120**, 92–104 (2014).
- 381 46. Zundel, M. et al. Thurston Island (West Antarctica) between Gondwana subduction
382 and continental separation: A multistage evolution revealed by apatite
383 thermochronology. *Tectonics* **38**, 878–897 (2019).
- 384 47. Müller, R. D., Gohl, K., Cande, S. C., Goncharov, A. & Golynsky, A. V. Eocene to
385 Miocene geometry of the West Antarctic rift system. *Australian Journal of Earth*
386 *Sciences* **54**, 1033–1045 (2007).
- 387 48. Harbert, R. S. & Nixon, K. C. Climate reconstruction analysis using coexistence
388 likelihood estimation (CRACLE): A method for the estimation of climate using
389 vegetation. *American Journal of Botany* **102(8)**, 1277–1289 (2015).
- 390 49. Poole, I., Cantrill, D. J. & Utescher, T. Reconstructing Antarctic palaeoclimate from
391 wood floras: a comparison using multivariate anatomical analysis and the

- 392 Coexistence Approach. *Palaeogeogr. Palaeoclimatol. Palaeoecol.* **222**, 95–121
393 (2005).
- 394 50. Francis, J. E. et al. 100 million years of Antarctic climate evolution: evidence from
395 fossil plants. In: Cooper, A. K. & Barrett, P. et al. (eds.) *Antarctica: A Keystone in a*
396 *Changing World. Proceedings of the 10th International Symposium on Antarctic Earth*
397 *Sciences. USGS Santa Barbara, California, August 26 to September 1, 2007, The*
398 *National Academies Press, Washington D.C., USA, pp. 19–27 (2007).*
- 399 51. Bauersachs, T., Rochelmeier, J. & Schwark, L. Seasonal lake surface water
400 temperature trends reflected by heterocyst glycolipid-based molecular thermometers.
401 *Biogeosciences* **12**, 3741–3751 (2015).
- 402 52. Ladant, J. L. & Donnadieu, Y. Paleogeographic regulation of glacial events during the
403 Cretaceous supergreenhouse. *Nat. Comm.* **7**, doi:10.1038/ncomms12771, (2016).
- 404 53. Upchurch, G. R. jr., Kiehl, J., Shields, C., Scherer, J. & Scotese, C. Latitudinal
405 temperature gradients and high-latitude temperatures during the latest Cretaceous:
406 Congruence of geologic data and climate models. *Geology* **43**, 683–686 (2015).
- 407 54. Farnsworth, A. et al. Climate sensitivity on geological timescales controlled by non-
408 linear feedbacks and ocean circulation. *Geophys. Res. Lett.* **46**,
409 doi:10.1029/2019GL083574 (2019).
- 410 55. IPCC. IPCC Special Report on the Ocean and Cryosphere in a Changing Climate.
411 Pörtner, H. O. et al. (eds.), in press.
412 [https://www.ipcc.ch/site/assets/uploads/sites/3/2019/12/SROCC_FullReport_FINAL.p](https://www.ipcc.ch/site/assets/uploads/sites/3/2019/12/SROCC_FullReport_FINAL.pdf)
413 [df](https://www.ipcc.ch/site/assets/uploads/sites/3/2019/12/SROCC_FullReport_FINAL.pdf) (2019).

414
415 *Figure captions*

416 Figure 1: Setting of *MARUM-MeBo70* drill site PS104_20-2 on the Amundsen Sea
417 Embayment (ASE) shelf. a) The modern configuration of West Antarctica is placed in relation
418 to the reconstructed boundary between continental and oceanic crust (COB) at 84 Myr^{33,34}
419 (thick black lines). The pre-break up suture (dashed white line) indicates the position of the

420 reconstructed Zealandian and West Antarctic COBs prior to initial break-up starting at ~90
421 Myr³³. Orange circles mark the locations of other outcrops of mid-Cretaceous sedimentary
422 strata^{13–17}. b) Seismic reflection profile NBP9902-11²³ (A-B) crossing drill site 20-2: orange
423 bar indicates drilled core length. The profile position is indicated in “a”. The drill hole
424 penetrated Amundsen Sea shelf unconformity ASS-u1, which separates seismic units ASS-1
425 and ASS-2²⁶. Interpretation of seismostratigraphic units and unconformities is based on both
426 previous work²⁶ and this study. Pitt Island belongs to the Chatham Island group of New
427 Zealand. PB: Prydz Bay; ChR: Chatham Rise. Shelf bathymetry and sub-ice topography data
428 derive from refs. 20 and 21.

429

430 Figure 2: Multi-proxy parameter reconstruction of cores 9R and 10R at site PS104_20-2. The
431 *MARUM-MeBo70* sea floor drill rig drilled 30.7 m into the seafloor and recovered 5.91 m of
432 core length. The lower ~3 m consist of a fossil root-bearing mudstone with a ~5 cm-thin layer
433 of brecciated lignite on top (from ~26.77 mbsf downwards) both of Turonian–Santonian age.
434 A Late Eocene or younger quartzitic sandstone overlies the lignite. The upper lignite
435 boundary defines the impedance contrast between the underlying mudstone and overlying
436 quartzitic sandstone and likely coincides with the prominent regional unconformity ASS-u1²⁶
437 (see thick red line in Fig. 1b). Note the core break between 9R and 10R at 27.15 mbsf. (LS:
438 Linescan; CT: X-Ray computed tomography; Cl/St/Sd: Clay/Silt/Sand; TOC: Total organic
439 carbon; Gy/An/Pt/Br: Gymnosperms/Angiosperms/Pteridophytes/Bryophytes; x: Barren
440 palynomorph samples; Fe(Ca): Iron-carbonate; Bulk sediment ϵ_{Nd} values and $^{87}Sr/^{86}Sr$ ratios
441 (see Methods); TAR: Ratio of terrestrial and aquatic-sourced *n*-alkanes; C:N (mol.): molar
442 ratio of total organic carbon (TOC) to total nitrogen (TN); *: Zircon U-Pb age (45.5 Myr);
443 mbsf: meters below sea floor). Inferred ages are based on palynomorph biostratigraphy for
444 the mudstone and U/Pb ages of apatite and zircon grains for the sandstone (see text). Data
445 link to PANGAEA (DOI in progress):

446 <https://www.pangaea.de/tok/c29ccbd70a3a1dae9e4b4711c3b50cf25287a201>

447

448 Figure 3: Modern and mid-Cretaceous CO₂ sensitivity runs. Distribution of warmest mean
449 month temperatures (WMMT) (°C) for present (upper row: a-c) and mid-Cretaceous at 90
450 Myr (lower row: d-f) configurations for atmospheric CO₂ levels of 280, 560, 1120 ppm,
451 representing 1x, 2x and 4x pre-industrial CO₂ level of 280 ppm. The black triangle indicates
452 the approximate position of site PS104_20-2 (a–c: modern; d–f: Turonian–Santonian). g)
453 Modelled mid-Cretaceous WMMT (dashed coloured lines) and zonal mean temperatures (full
454 coloured lines) for different atmospheric CO₂ concentrations. The temperature estimates,
455 including their respective calibration error (2σ), were derived from the following proxies
456 referred to in ref. 5: terrestrial δ¹⁸O of vertebrate tooth enamel and/or pedogenic carbonate
457 (full squares), palaeobotanical data (full circles), fish enamel δ¹⁸O (open triangles), marine
458 calcareous fossil δ¹⁸O (open diamonds), and biomarkers (cross). Temperature estimates
459 from this study are indicated as a red full circle and cross, respectively.

460

461 Figure 4: Visual reconstruction of the West Antarctic Turonian–Santonian temperate
462 rainforest. The painting is based on palaeo-floral and environmental information inferred from
463 palynological, geochemical, sedimentological, and organic biomarker data obtained from
464 cores 9R and 10R at site PS104_20-2. The creation of the painting was further
465 complemented by published palaeo–topographic and palaeo–tectonic information^{24,26,33}
466 (Artist: James McKay, University of Leeds, UK; original size of painting: 83.8 x 41.5 cm).

467

468 *Acknowledgements*

469 We thank captain and crew of RV *Polarstern* Expedition PS104, as well as the MARUM-
470 *MeBo70* team for their support. The operation of the *MARUM-MeBo70* Sea Floor Drill Rig
471 was funded by the Alfred Wegener Institute (AWI) through its Research Program PACES II
472 Topic 3 and grant no. AWI_PS104_001, the MARUM Center for Marine Environmental
473 Sciences, the British Antarctic Survey through its Polar Science for Planet Earth programme,
474 and the Natural Environmental Research Council funded UK IODP programme. S. Wiebe, R.
475 Fröhling, N. Lensch, M. Seebeck, and H. Grobe are thanked for their help on board and in

476 the lab, respectively. The *Klinikum Bremen-Mitte* (A.-J. Lemke and C. Tiemann, *Gesundheit*
477 *Nord* Bremen) is acknowledged for providing facilities for computed core tomographies, and
478 M. Köhler (MKfactory, Germany) for preparing the thin sections. J. McKay (University of
479 Leeds) is thanked for creating and painting the Late Cretaceous West Antarctic
480 palaeoenvironment based on reconstructions presented here. J.P.K, G.K., K.G., J.M. G.U.-
481 N., O.E., C.G., T.R. and R.D. were funded by the AWI PACES II programme. J.P.K. and J.M.
482 were additionally funded through the Helmholtz Association (PD-201 & VH-NG-1101). UK
483 IODP funded participation of T.v.d.F., P.S.P. and S.M.B. in expedition PS104. J.T. was
484 funded through the Cluster of Excellence “The Ocean Floor – Earth’s Uncharted Interface” at
485 the University of Bremen.

486

487 *Author contributions*

488 J.P.K. led the study and together with U.S., T.B., C.-D.H., K.G. and G.K., conceived the idea
489 for the study and wrote the manuscript. J.P.K, T.B., C.-D.H., S.B., J.A.S., K.G., T.F, T.v.d.F.,
490 P.S.P., W.E., O.E., H.P. and T.R. collected the cores. J.P.K, C.-D.H., T.B. and G.K.
491 undertook the sedimentological and U.S. the palynological analyses. T.B. and G.K.
492 conducted the XRF scanning and processing of the cores. G.K. carried out the grain-size and
493 bulk mineralogical analyses. J.T. led the CT scanning, processing, and visualization. J.M.
494 performed the biomarker analyses together with Th.B. (heterocyst glycolipid
495 palaeothermometry). T.F. conducted the palaeomagnetic measurements. J.E.F., G.N., G.K.
496 and J.P.K. investigated the thin sections. W.E. analysed the clay mineral assemblages and
497 T.v.d.F. and P.S.P. measured bulk sediment Nd and Sr isotope compositions. K.G., R.D.L.,
498 and T.F. helped determining the palaeolatitude of the drill site. G.L. and I.N. undertook the
499 modelling with COSMOS. M.Z. and C.S. provided the U/Pb age constraints. U.S. and F.S.
500 performed the bioclimatic analyses. J.P.K., T.B., C.-D.H., S.B., T.F., W.E., J.A.S., O.E., O.E.,
501 H.P., T.R. and R.D. helped sampling and scanning the cores. K.G., G.U.-N. and R.D.L.
502 undertook the seismic pre-site survey. All members of the Expedition PS104 Science Team
503 helped in pre-site survey investigations, core recovery, on-board analyses and/or shore-

504 based measurements. K.G., G.K., C.-D.H., G.U.-N., T.B. and R.D.L. acquired funding,
505 proposed, and planned RV *Polarstern* expedition PS104. All co-authors commented on the
506 manuscript and provided input to its final version.

507

508 *Author information*

509 Reprints and permissions information is available at www.nature.com/reprints. The authors
510 declare no competing financial interests. Readers are welcome to comment on the online
511 version of the paper. Correspondence and requests for materials should be addressed to
512 J.P.K. (Johann.Klages@awi.de).

513

514

515

516

517

518

519

520

521

522

523

524

525

526

527

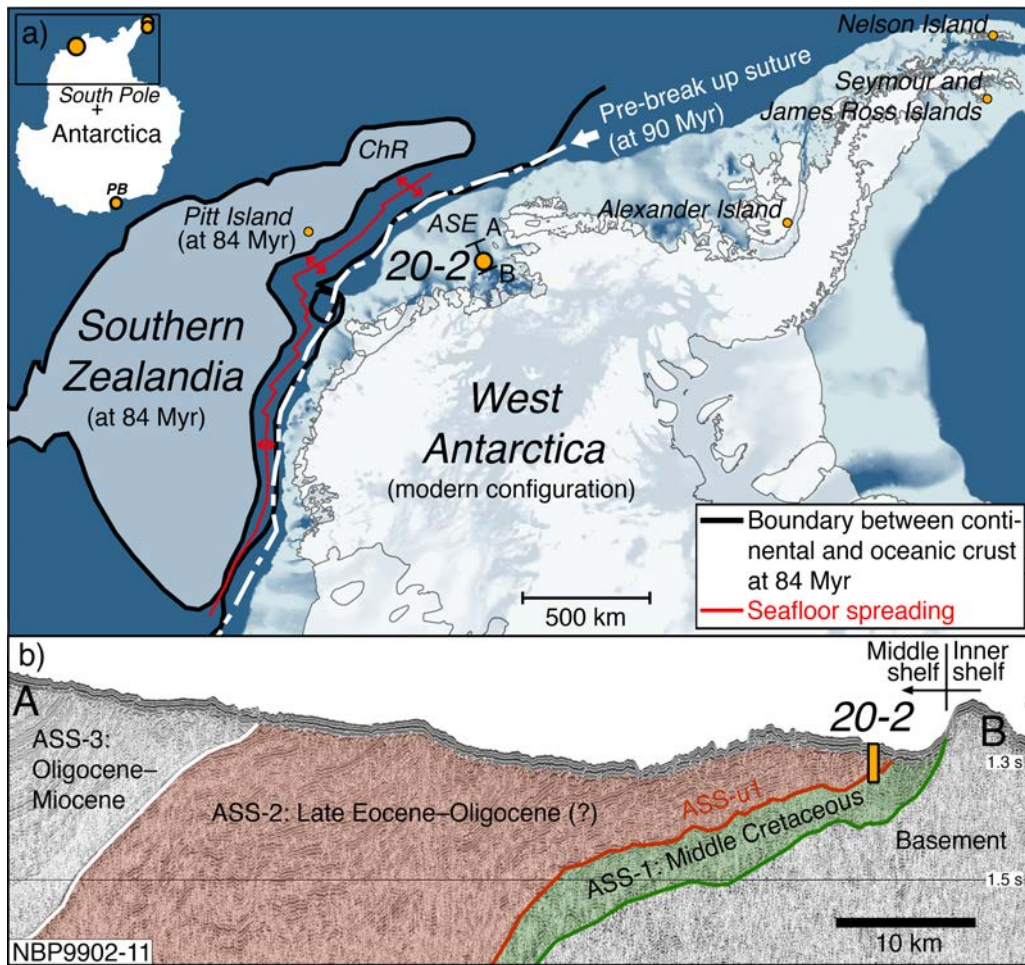
528

529

530

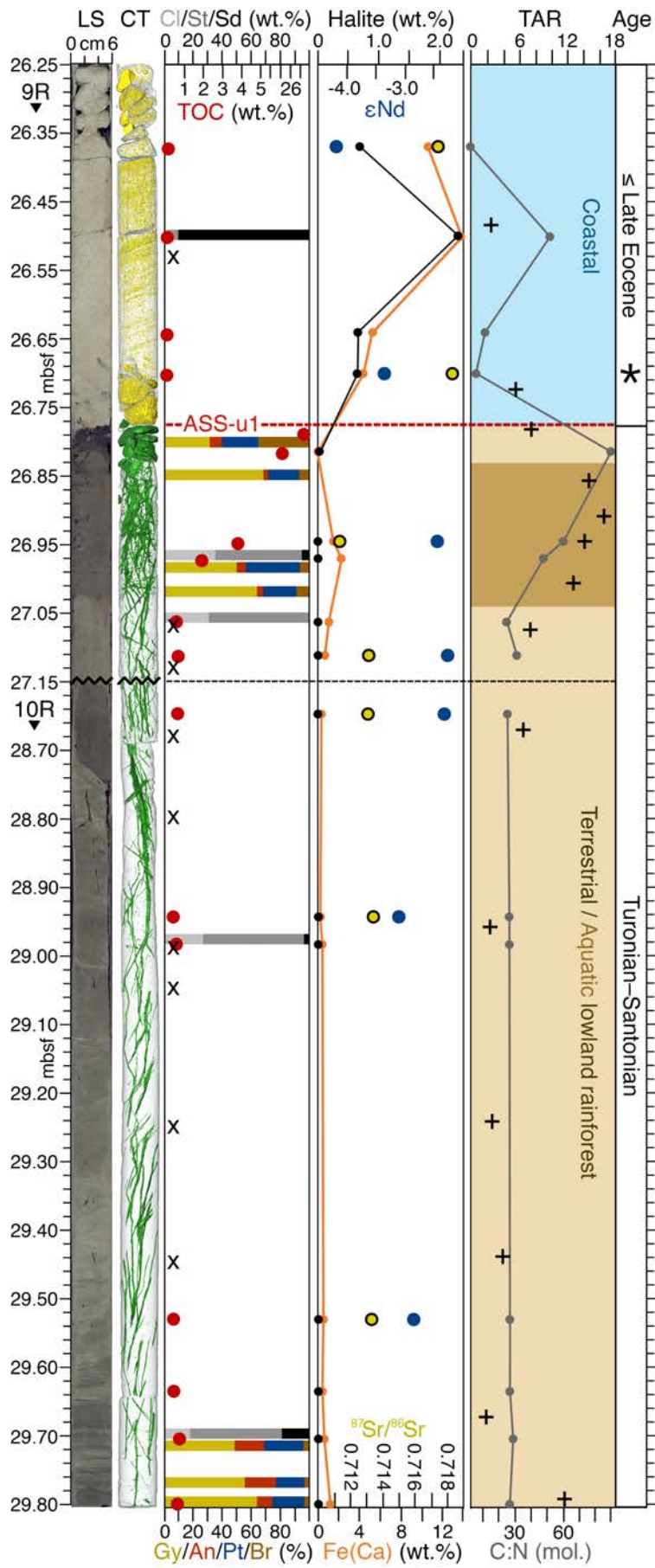
531

532 Figure 1



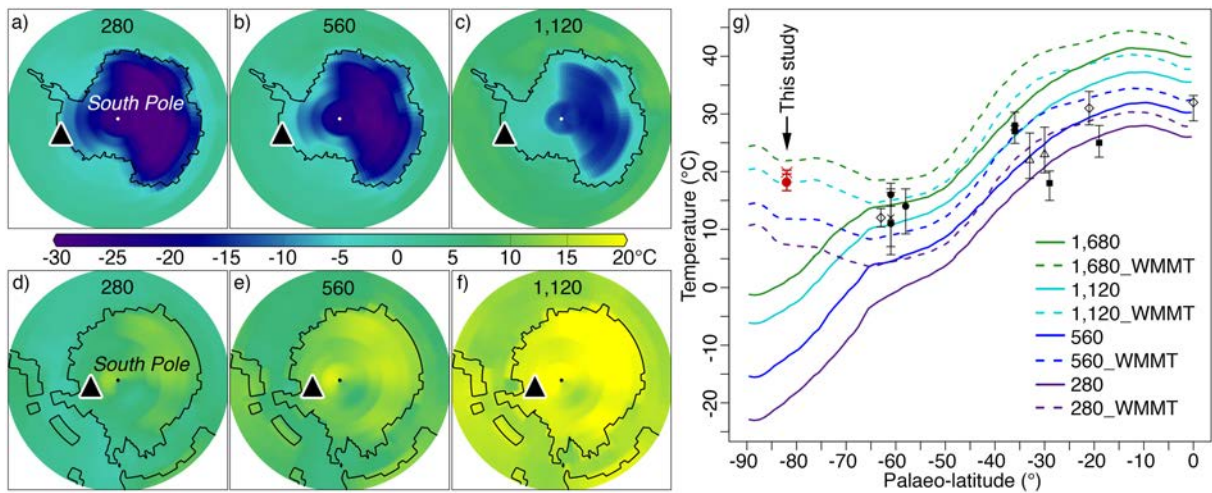
533
534
535
536
537
538
539
540
541
542
543
544
545
546

547 Figure 2



548

549 Figure 3



550

551

552 Figure 4



553

554

555 **Science Team of Expedition PS104:**

556 Afanasyeva, V., VNIIOkeangeologie, St. Petersburg, Russia

557 Arndt, J. E., Alfred-Wegener-Institut, Helmholtz-Zentrum für Polar- und Meeresforschung,
558 Bremerhaven, Germany

559 Ebermann, B., Technische Universität Dresden, Dresden, Germany

560 Gebhardt, C., Alfred-Wegener-Institut, Helmholtz-Zentrum für Polar- und Meeresforschung,
561 Bremerhaven, Germany

562 Hochmuth, K., Alfred-Wegener-Institut, Helmholtz-Zentrum für Polar- und Meeresforschung,
563 Bremerhaven, Germany, now at: School of Geology, Geography and the Environment,
564 University of Leicester, Leicester, UK

565 Küssner, K., Alfred-Wegener-Institut, Helmholtz-Zentrum für Polar- und Meeresforschung,
566 Bremerhaven, Germany

567 Najman, Y., Lancaster Environment Centre, Lancaster University, Lancaster, UK

568 Riefstahl, F., Alfred-Wegener-Institut, Helmholtz-Zentrum für Polar- und Meeresforschung,
569 Bremerhaven, Germany

570 Scheinert, M., Technische Universität Dresden, Dresden, Germany

571

572 *Methods*

573 **Sea Floor Drill Rig *MARUM-MeBo70***

574 The sea floor drill rig *MARUM-MeBo70* is a robotic drill rig that was deployed on the seabed
575 and remotely controlled from RV *Polarstern* during expedition PS104²². Detailed information
576 about the drill rig and its operation is published in ref. 27.

577

578 **X-ray computed tomography**

579 Whole rounds of *MeBo* core PS104_20-2 were scanned by a *Toshiba Aquilion 64*TM
580 computer tomograph (CT) at the hospital *Klinikum Bremen-Mitte*, with an X-ray source
581 voltage of 120 kV and a current of 600 mA. The CT scans have a resolution of 0.351 mm in
582 x- and y-direction and 0.5 mm resolution in z-direction (resolution of scaled reconstruction:
583 0.195 x 0.195 x 0.3 mm). Images were reconstructed using Toshiba's patented helical cone
584 beam reconstruction technique. The obtained CT data were processed using the ZIB edition
585 of the *Amira* software (version 2017.39)⁵⁶. Within *Amira*, the CT scans of the core sections
586 were merged when necessary and core liners, including about 2 mm of the core rims, were
587 removed from the dataset until all marginal artefacts from the coring process were removed.
588 Subsequently, all clasts > ~1 mm, root-traces (where present) and matrix sediment were
589 segmented with the (marker-based) watershed tool of the *Segmentation Editor*. Markers

590 were predominantly set by density thresholding. Holes within clasts after the watershed
591 segmentation were added to the clasts with the *selection fill* tool. Only in exceptional cases,
592 markers were segmented by hand.

593

594 **Palynology**

595 Between 2 and 6 g of dry weight sediment per sample were processed at Northumbria
596 University, following standard palynological techniques, including sieving (10 µm) and acid
597 treatment with 10% HCl (Hydrochloric acid) and cold 38% HF (Hydrofluoric acid). The
598 processed residue was transferred to microscope slides using glycerine jelly as a mounting
599 medium, and 2–3 slides were analysed per sample at 400x magnification. Of the 17 samples
600 analysed for pollen and spores, 7 were productive, and total counts range from 340 to 360
601 pollen and spores per sample (Extended Data Figs. 2, 3; Extended Data Table 1). Pollen
602 concentrations increase from an average of ~6,500 grains/g sediment in the lower three
603 samples to 61,000–121,500 grains/g at the top. We could not identify any reworking of
604 palynomorphs. Percentages were calculated based on the sum of total pollen and spores. 65
605 pollen and spore taxa were identified from the literature^{57–59} (Extended Data Table 3). All
606 samples contained a high morphological diversity of *Podocarpus* pollen, which we classified
607 as *Podocarpidites* undiff., as many of these grains were either folded or damaged and were
608 therefore unidentifiable beyond family level. Marine dinoflagellate cysts were absent in all
609 samples.

610

611 **Palynomorph-based climate reconstructions (Bioclimatic analysis)**

612 We reconstructed terrestrial mean annual temperature (MAT), precipitation (MAP) and mean
613 warmest month temperature (WMMT) using the Nearest Living Relative (NLR) approach.
614 The NLR approach uses the climatic requirements of the NLR of fossil taxa to reconstruct the
615 past climatic range and assumes that the climatic requirements of the fossil taxa are similar
616 to those of their NLR (Extended Data Table 2). NLR approaches use the presence or
617 absence of individual taxa in fossil assemblage rather than relative abundance, which

618 reduces the likelihood of taphonomic biases. This facilitates, to some extent, the
619 reconstruction of past non-modern analogue climates and environments⁶⁰. NLR-based
620 temperature estimates are generally in good agreement with estimates from geochemical
621 and other palaeobotanical methods, including the Climate Leaf Analysis Multivariate Program
622 (CLAMP) and Leaf Margin Analysis^{61–67} providing confidence in the utility of the method for
623 the reconstruction of “deep-time” climates.

624 However, quantitative climate estimates from the fossil plant record of “deep-time” geological
625 intervals are always accompanied by large uncertainties. Incorrect use of outliers and fossil
626 taxa with ambiguous affinity can result in erroneous climate estimates⁶⁸. One of the greatest
627 weaknesses that affects all NLR approaches is the assumption of uniformitarianism, namely
628 that the climate tolerances of modern species can be extended into the past. This assumption
629 inevitably introduces uncertainty that increases with the age of the geological formation⁶⁹. In
630 order to statistically constrain the most likely climatic co-occurrence envelope, we combined
631 the NLR approach with the probability density function (PDF) method^{70–72}. In contrast to other
632 NLR methods, such as the Coexistence Approach, the PDF method has the advantage that it
633 statistically constrains the most likely climatic co-occurrence envelope, thereby offering a
634 solution to mathematically reduce the potential impact of wrongly defined climate tolerance on
635 upper and lower limits of palaeoclimatic estimates. In order to further reduce uncertainties
636 caused by potentially wrong identification of NLR, we removed fossil taxa with potentially
637 ambiguous affinity or very rare occurrence in the fossil record (Extended Data Table 2). This
638 includes *Microcachrydites antarcticus*, a taxon abundant and widespread in the fossil Antarctic
639 record, with the NLR *Microcachrys tetragona*, the sole species of the genus *Microcachrys*, that
640 nowadays is endemic to Tasmania. Another example is *Peninsulapollis gillii* with close links to
641 the modern genus *Beauprea*, and endemic to New Caledonia. In both cases we used the
642 family, Podocarpaceae and Proteaceae, respectively, rather than the genus or species as the
643 NLR.

644 To generate the paleoclimate estimate, we followed the procedure described in refs. 59 and
645 63. We first identified the bioclimatic envelope for each NLR by cross-plotting their modern

646 distribution from the Global Biodiversity Information Facility (GBIF)⁷³ with the gridded
 647 WorldCLIM climate surface⁷⁴ using the “dismo” package⁷⁵ in R. We then filtered the dataset
 648 and removed redundant data, “exotic” occurrences (such as garden plants) as well as
 649 multiple entries per climate grid cell to avoid the climatic probability function becoming highly
 650 slanted towards that location⁷⁶. Before establishing the probability density functions,
 651 bootstrapping was applied to test the robustness of the dataset, which is of particular interest
 652 for taxa with only few modern occurrences. Following the bootstrapping, we calculated the
 653 likelihood (f) of a taxon (t) occurring at value (x) for a certain climatic variable by using the
 654 mean (μ) and standard deviation (σ) of the modern distribution range of each taxa^{65,70}.

$$655 \quad f(x)_t = \frac{1}{\sqrt{2\pi\sigma_x^2}} e^{-\frac{(x-\mu_x)^2}{2\sigma_x^2}}$$

656
 657 Since the separate reconstruction of climate ranges for each variable can lead to bioclimatic
 658 envelopes that include intervals, where no modern-day occurrence of taxon t is observed⁶⁵,
 659 we calculated joint likelihood PDFs for each combination of climate variables MAT, MAP and
 660 WMMT using the correlation coefficient $p(x, y)$:

$$662 \quad f(x, y)_t = \frac{1}{2\pi\sigma_x\sigma_y\sqrt{1-p^2}} e^{-\frac{1}{2(1-p^2)}\left(\frac{(x-\mu_x)^2}{2\sigma_x^2} + \frac{(y-\mu_y)^2}{2\sigma_y^2} - 2p\frac{(x-\mu_x)(y-\mu_y)}{\sigma_x\sigma_y}\right)}$$

663
 664 After assessing if all bioclimatic envelopes share a coexistence interval, the climate
 665 estimates of the NLR assemblage were reconstructed by multiplying the individual joint
 666 likelihoods of taxa $f(x, y)_{t1} \dots f(x, y)_{tn}$ with each other:

$$668 \quad f(x, y)_{Combined} = f(x, y)_{t1} \times f(x, y)_{t2} \times \dots \times f(x, y)_{tn}$$

669
 670 In order to constrain the core distribution of a group, we determined the range of one ($f(x,$
 671 $y)_{relative} = 0.157$) and two standard deviations ($f(x, y)_{relative} = 0.023$) from the occurrence within
 672 a group with $f(x, y)_{max}$ representing the most likely climate conditions⁷⁶.

673

$$674 \quad f(x,y)_{relative} = \frac{f(x,y)}{f(x,y)_{max}}$$

675

676 For our bioclimatic analysis we used all pollen and spore taxa that could be related to an
677 NLR, following ref. 59 (Extended Data Table 2). Climatic ranges are indicated with their $\pm 2 \sigma$
678 range. For our record we calculated mean annual temperatures of $12.8 \pm 2.2^\circ\text{C}$, warmest
679 mean month temperatures of $18.4 \pm 1.9^\circ\text{C}$, and mean annual precipitation of $1,120 \pm 330$
680 mm/a. It should be noted that the ranges of these values show the mathematical error and
681 not the real range, which might result from the uncertainties of using an NLR approach
682 method. To avoid misunderstandings, we therefore indicated in the main text the pollen-
683 based climate estimates without 2σ ranges.

684

685 **Organic geochemistry**

686 Freeze-dried and homogenized sediment samples were extracted by means of
687 ultrasonication using a dichloromethane:methanol mixture (2:1, v:v). After centrifugation, the
688 total lipid extract was dried by rotary evaporation. The extraction was repeated twice. The
689 combined total lipid extract was fractionated using silica open-column chromatography and
690 hexane as eluent to obtain apolar lipids. Hydrocarbons were analysed using an HP gas
691 chromatograph 6890 (30 m DB-5MS column, 0.25 mm diameter, 0.25 μm film thickness).
692 The identification of *n*-alkanes, pristane, and phytane was based on comparison of their
693 retention times with those of reference compounds that were run on the same instrument.
694 The terrigenous-aquatic-ratio (TAR⁷⁷) was calculated using peak areas of long-chain (*n*-C₂₇,
695 *n*-C₂₉, *n*-C₃₁) against short-chain (*n*-C₁₅, *n*-C₁₇, *n*-C₁₉) alkanes. The carbon preference index
696 (CPI) was calculated as follows⁴⁰:

697

$$698 \quad (1) \text{ CPI} = 2 * (n\text{-C}_{23} + n\text{-C}_{25} + n\text{-C}_{27} + n\text{-C}_{29}) / (n\text{-C}_{22} + 2 * (n\text{-C}_{24} + n\text{-C}_{26} + n\text{-C}_{28}) + n\text{-C}_{30}).$$

699

700 **Heterocyst glycolipid palaeothermometry**

701 Sediment samples from the coastal sandstone (9R, 50-52 cm; 2676 cmbsf) and the
702 carbonaceous mudstone (9R, 76.5–78 cm; 27.02 mbsf; 10R, 60–62 cm; 29.21 mbsf) were
703 lyophilized and ground to fine sediment powder using a solvent-cleaned agate pestle and
704 mortar. Between 20.1 and 29.7 g of sediment was extracted using a modified Bligh and Dyer
705 procedure⁷⁸. Briefly, the cell material was extracted ultrasonically thrice for 10 min each in a
706 solvent mixture of MeOH, DCM and phosphate buffer (2:1:0.8; v:v:v). After each sonication
707 step, the solvent mixture was centrifuged at 1,500 x g for 3 min and the supernatant
708 transferred to a centrifuge tube. The combined supernatants were phase separated by
709 adding DCM and phosphate buffer to a final solvent ratio of 1:1:0.9 (v:v:v). The organic
710 bottom layer was collected in a round bottom flask and reduced under vacuum using a rotary
711 evaporator. Each Bligh and Dyer extract (BDE) was transferred to a pre-weighed vial using
712 DCM:MeOH (1:1, v:v) and dried under a gentle stream of N₂. Prior to analysis, all BDEs were
713 re-dissolved in a solvent mixture of *n*-hexane:2-propanol:H₂O (72:27:1; v:v:v) to a
714 concentration of 8 mg/ml. In order to test for possible cross contamination during sample
715 preparation a blank was included in each batch and treated as a regular sample.

716 High performance liquid chromatograph coupled to electrospray ionisation tandem mass
717 spectrometry (HPLC/ESI-MS²) was performed on the BDEs following the analytical
718 procedure given by ref. 79 to establish heterocyst glycolipid (HG) distribution patterns and
719 relative abundances. Separation of HGs was achieved using a Waters Alliance 2690 HPLC
720 system fitted with a Phenomenex Luna NH₂ column (150 x 2 mm; 3 μm particle size) and a
721 guard column of the same material. Both were maintained at a constant temperature of 30°C.
722 The applied gradient profile was as follows: 95% A/5% B to 85% A/15% B in 10 min.
723 (isocratic for 7 min) at 0.5 ml min⁻¹, followed by back flushing with 30 % A/70% B at 0.2 ml
724 min⁻¹ for 25 min. and re-equilibrating the column with 95% A/5% B for 15 min. Solvent A was
725 *n*-hexane:2-propanol:HCO₂H:14.8 M NH₃ aq. (79:20:0.12:0.04; v:v:v) and Solvent B was 2-
726 propanol:water:HCO₂H:14.8 M NH₃ aq. (88:10:0.12:0.04; v:v:v).

727 Heterocyst glycolipids were detected using a Micromass Quattro LC triple quadruple mass
728 spectrometer equipped with an electrospray ionisation (ESI) interface and operated in

729 positive ion mode. Source conditions were as given in ref. 80. All BDEs were analysed in
730 multiple reaction monitoring (MRM) mode to achieve maximum specificity and HGs identified
731 based on comparison of retention times with those of HGs in cultured cyanobacteria as well
732 as published mass spectral information^{81–85}. HGs were monitored using the following
733 transitions: m/z 547 \rightarrow 415 (pentose HG₂₆ diol), m/z 603 \rightarrow 471 (pentose HG₃₀ diol), m/z 619
734 \rightarrow 487 (pentose HG₃₀ triol), m/z 647 \rightarrow 515 (pentose HG₃₂ triol), m/z 561 \rightarrow 415
735 (deoxyhexose HG₂₆ diol), m/z 575 \rightarrow 413 (HG₂₆ keto-ol), m/z 577 \rightarrow 415 (HG₂₆ diol), m/z 603
736 \rightarrow 441 (HG₂₈ keto-ol), m/z 605 \rightarrow 443 (HG₂₈ diol), m/z 619 \rightarrow 457 (HG₂₈ keto-diol), m/z 621
737 \rightarrow 459 (HG₂₈ triol), m/z 635 \rightarrow 459 (methylated hexose HG₂₈ triol), m/z 647 \rightarrow 485 (HG₃₀
738 keto-diol), m/z 649 \rightarrow 487 (HG₃₀ triol), m/z 675 \rightarrow 513 (HG₃₂ keto-diol), m/z 677 \rightarrow 515 (HG₃₂
739 triol) and quantified by integrating peak areas using the QuanLynx application software.
740 Surface water temperatures (SWTs) during the deposition of the coastal Eocene sandstone
741 were re-constructed using the HDI₂₆ (heterocyst diol index of 26 carbon atoms) and HDI₂₈
742 (heterocyst diol index of 28 carbon atoms) lipid palaeothermometers as described by ref. 51.
743 As the HG content of the swampy palaeoenvironment exclusively consisted of HG₃₀ triols
744 and HG₃₀ keto-diol (Extended Data Fig. 4), which are specific for cyanobacteria forming
745 benthic microbial mats⁸³, we here applied the HTI₃₀ (heterocyst triol index of 30 carbon
746 atoms) to the mudstone sequence. This index is defined as follows:

$$747 \text{ HTI}_{30} = \text{HG}_{30} \text{ triol} / (\text{HG}_{30} \text{ triol} + \text{HG}_{30} \text{ keto-diol})$$

748 The HTI₃₀ was transferred to absolute temperatures using a surface sediment calibration
749 obtained from a large set of East African lakes ($n = 47$) located on an altitudinal transect from
750 615 to 4504 masl and SWTs ranging from 5.7 to 27.9°C. In this setting, the HTI₃₀ showed a
751 strong linear correlation with SWT, which is expressed in the equation below (Bauersachs,
752 unpublished data):

$$753 \text{ SWT} = (\text{HTI}_{30} / 0.0249) - (0.2609 / 0.0249)$$

754 Independent conformation for the robustness of the HG-based temperature reconstruction is
755 obtained by comparing HG distribution patterns and HTI₃₀ values in the mudstone sequence
756 with those reported for an axenic culture of the heterocystous cyanobacterium *Scytonema*
757 sp. PCC 10023 (ref. 85). This cyanobacterium exclusively contains HG₃₀ triols and HG₃₀
758 keto-diols. The above transfer function predicts a HTI₃₀ of ~0.88 for the culture grown at an
759 ambient temperature of 25°C, which is in the same order of magnitude as the HTI₃₀
760 calculated using the relative abundances of the major HG₃₀ triol and HG₃₀ keto-diol isomers
761 reported in ref. 85.

762

763 **Grain-size analyses**

764 A set of discrete samples was wet sieved at 2 mm and 63 µm to separate the grain-size
765 classes gravel, sand, and mud. The < 63 µm (mud) suspension was separated into silt (2 to
766 63 µm) and clay (< 2 µm) using settling velocity (Stokes' Law) in Atterberg tubes.

767

768 **Clay mineral analyses**

769 An aliquot of the clay fraction was used to determine the relative contents of the clay
770 minerals smectite, illite, chlorite, and kaolinite using an automated powder diffractometer
771 system Rigaku MiniFlex with CoK α radiation (30 kV, 15 mA) at the Institute for Geophysics
772 and Geology (University of Leipzig). The clay mineral identification and quantification
773 followed standard X-ray diffraction methods⁸⁶.

774

775 **Bulk sediment composition**

776 Total carbon (TC) and total nitrogen (TN) were analysed with an Elementar Vario EL III. Total
777 organic carbon (TOC) contents were determined after removal of the total inorganic carbon
778 (TIC, carbonates) with HCl using an ELTRA CS-2000. Carbonate content was calculated by
779 subtracting the TOC from the TC and multiplying the difference (TIC) by 8.33, i.e. the ratio
780 between the molecular weights of CaCO₃ and C. The TOC:TN (C:N) ratio was calculated on
781 a molar basis.

782 The mineralogical composition of the milled bulk sediment was analysed semi-quantitatively
783 with X-ray diffraction using peak intensities and area ratios analysed with the MacDiff
784 program⁸⁷. For the Fe(Ca)-carbonates the peak intensities for ankerite (at 2.9 Å) and siderite
785 (at 2.791 Å) were used and summed up as percentages for Fe(Ca)-carbonates (ankerite and
786 siderite) in relation to the absolute % of other carbonates (calcite, Mg-calcite, and dolomite).

787

788 **Thin sections**

789 After drying the untreated soft sediment in the fridge for 2–3 days, the sediment was dried at
790 room temperature (20–22°C) for another 2–3 days. During that time the sediment was
791 checked daily for crack formation. Under low pressure, the sediment was impregnated
792 stepwise in a vacuum exicator with epoxy araldite 2020 resin until full coverage of the
793 sample. After complete hardening, the bottom of the sample was ground by a Tegrapol with
794 silicon carbid (SiC) paper sizes from 80 to 800 – depending on sediment characteristics –
795 and a maximum of 150 rotations per minute until reaching the sediment surface. The glasses
796 for covering the thin sections with a thickness of 3 mm and a diameter of 35x120 mm were
797 ground with a 9-micron fraction SiC paper to achieve both grip and an even surface
798 (alternative machine system: Logitech LP50 auto). Then the sample was attached to the
799 glass with the same resin used for impregnation by a pressure block. Afterwards, the surface
800 of the glass was cleaned and labelled with a diamond pen. Most samples were then cut by a
801 WOCO 50 diamond saw for achieving 250 µm-thick sediment stripes on the glass, before
802 grounding with SiC paper or the Logitech LP50 to reach a thickness of 30 µm. Some
803 sections were covered with 150 µm-thick glasses, for which an ultraviolet resin (cyanacrylate)
804 was used. Most sections remained uncovered for Raman and SEM-EDX spectroscopy.

805 Finally, all thin sections were cleaned with ethanol. The set of thin sections was prepared by
806 MKfactory (Stahnsdorf, Germany).

807

808 **Palaeomagnetic measurements**

809 Five discrete samples were taken with variable spacing from cores 9R and 10R of core
810 PS104_20-2 for palaeomagnetic investigations using plastic boxes with inner dimensions of
811 2×2×2 cm. Directions and intensities of natural remanent magnetization (NRM) were
812 measured on a cryogenic magnetometer (model 2G Enterprises 755 HR). Subsequent
813 alternating field demagnetization of NRM involved 15 steps to a maximum AF intensity of 100
814 mT. A detailed vector analysis⁸⁸ was applied to the results in order to determine the
815 characteristic remanent magnetization (ChRM) of each sample and to unravel its magnetic
816 polarity. Samples showing no systematic demagnetization pattern were excluded from further
817 interpretation.

818

819 **Palaeoclimate modelling**

820 We use the COSMOS model (see Code availability) in a coupled atmosphere-ocean
821 configuration with fixed vegetation. The atmosphere component ECHAM5 is run in a T31/L19
822 resolution⁸⁹. It consists of 19 vertical layers and has a horizontal resolution of ~3.75°. The
823 ocean component MPI-OM runs in GR30/L40 configuration⁹⁰. It has a formal horizontal
824 resolution of 3.0° x 1.8° and consists of 40 unequal vertical layers. The high-resolution
825 hydrological discharge model is a part of ECHAM5⁹¹ while MPI-OM includes a dynamic-
826 thermodynamic sea-ice model utilizing a viscous-plastic rheology⁹². Climate simulations were
827 run for present and mid-Cretaceous configurations under different CO₂ levels in the
828 atmosphere. Other greenhouse gases (such as CH₄ and N₂O) were set to pre-industrial (PI)
829 level. In the mid-Cretaceous simulations, we employ published paleogeography⁹³ and
830 vegetation⁹⁴ as well as no ice sheets on both hemispheres. The orbital configurations in all
831 Cretaceous experiments were fixed at 800 common era (CE) and hence represent values from
832 the beginning of externally forced simulation from 800 to 1,800 CE (so called millennial run).
833 The solar constant was reduced by 1% for the mid-Cretaceous experiments relative to the
834 present-day value. The simulations with 1x and 2x PI CO₂ levels were run for 9,200 and 9,000
835 years, respectively, while 10,600 years for 4x PI CO₂ (ref. 95). All simulations reached
836 equilibrium at the surface. The experiment with 6x PI CO₂ level had a slightly different

837 atmospheric land-sea mask than the other three simulations. It was run for ~500 years and
838 was not in a full equilibrium at the surface⁵. The pre-industrial control simulation was run for
839 ~7,500 years. The simulations with 2x and 4x PI CO₂ levels were branched off from 1x PI
840 simulation from the year 6,800 and were further run for 700 years. The simulations reach either
841 full or quasi equilibrium at the surface. For the analyses the mean was taken over the last 100
842 years of each simulation. The model has been successfully applied previously for scientific
843 questions focusing on the Quaternary^{96,97}, Neogene^{98–100}, Palaeogene^{101,102}, Late Cretaceous⁵
844 as well as estimates of future climate^{100,103}.

845

846 **Sr and Nd isotopic measurements**

847 A total of seven samples were selected for processing from cores 9R and 10R at site
848 PS104_20-2. A detailed method description that was applied for determining their Sr and Nd
849 isotopic compositions is given in ref. 104.

850

851 **Zircon and apatite U-Pb geochronology**

852 The youngest detrital zircon and apatite U-Pb ages obtained from the cores 2R (sample AWI-
853 35 at 9.9 mbsf) and 9R (sample AWI-25 at 26.7 mbsf) were used for constraining maximum
854 deposition ages of the sandstone. The samples yielded Eocene apatite (n=2) and zircon (n=1)
855 ages. The single Eocene zircon grain yields a Concordia age of 45.5±2.0 Myr (Extended Data
856 Fig. 1a). The apatite grains all yield analyses discordant in U-Pb isotopic space due to the
857 presence of common-Pb (Pb_c; i.e. Pb incorporated during crystallisation as opposed to
858 radiogenic Pb* generated *in-situ* by radionuclide decay). For single-grain ages a terrestrial Pb-
859 isotope evolution model¹⁰⁵ was used for an initial estimate of ²⁰⁷Pb_c/²⁰⁶Pb_c, followed by an
860 iterative approach to the ²⁰⁷Pb-based corrected age calculation¹⁰⁶.

861 As only two Eocene single-grain apatite ages are reported, calculation of an array age would
862 not normally be indicated. However, comparison of the trace element chemistry (REE-Sr-Y) to
863 an apatite compositional reference library¹⁰⁷ indicates both Eocene grains are chemically as
864 well as chronologically indistinguishable (Extended Data Fig. 1b), increasing the likelihood of

865 a common source. Therefore, the two youngest apatite grains from AWI-35 were jointly
866 regressed with the range of $^{207}\text{Pb}_c/^{206}\text{Pb}_c$ values (0.834 ± 0.018) for West Antarctic crystalline
867 basement¹⁰⁸ (Extended Data Fig. 1a) to obtain a lower-intercept age of 39.3 ± 3.8 Myr (MSWD
868 = 0.99), similar to the independently-obtained single-grain Concordia age of 45.5 ± 2.0 Myr
869 yielded by the youngest zircon from AWI-25. A Lutetian maximum deposition age (ca. 43 Myr)
870 for AWI-35 and AWI-25 is therefore indicated.

871 Pure apatite and zircon separates were handpicked from the non-magnetic heavy mineral 63-
872 315 μm size fraction, mounted in epoxy resin, ground to reveal internal surfaces, and polished.
873 Virtually no sample bias was introduced by grain selection because in most cases all observed
874 mineral grains were picked as the amount of sample material was very small. All U-Pb analyses
875 were carried out using a Photon Machines Analyte Excite 193 nm ArF excimer laser-ablation
876 system with a HelEx 2-volume ablation cell coupled to an Agilent 7900 ICPMS at the
877 Department of Geology, Trinity College Dublin, Ireland. Laser fluence was 2.5 J cm^{-2} with a
878 repetition rate of 15 Hz and analysis time of 20 s, followed by an 8 s pause to allow for signal
879 washout and a subsequent baseline measurement. Spot sizes of 47 μm and 24 μm were
880 employed for apatite and zircon respectively, in separate analytical sessions.

881 Data reduction employed the Vizual_Age and VisualAge_UComPbine data reduction schemes
882 (DRS) for Iolite for zircon and apatite, respectively^{109–111}. Each DRS corrects for intra-session
883 analytical drift, mass bias, and downhole fractionation using a user-specified fractionation
884 model based on measurements of the primary standard; additionally, VisualAge_UComPbine
885 permits the presence of a variable Pb_c content in a primary age standard to be corrected for
886 using a known initial $^{207}\text{Pb}_c/^{206}\text{Pb}_c$ value. Final U-Pb age calculations were made using the
887 Isoplot add-in for Excel¹¹².

888 Single-grain zircon U-Pb Concordia ages were calculated, and analyses with probability of
889 concordance < 0.001 were rejected¹¹². The primary standard was Plešovice zircon; the GZ7
890 and 91,500 zircons were utilised as secondary standards and treated as unknowns during data
891 reduction and age calculation¹¹³, yielding Concordia ages of 530.1 ± 3.7 Myr and 1060.4 ± 6.8
892 Myr, respectively.

893 For apatite analyses, Madagascar apatite was employed as the primary standard and McClure
894 Mountain and Durango apatites were employed as secondary standards^{114,115}. Pb_c in the
895 secondary standards was corrected for using fixed initial ratios, yielding weighted mean ages
896 of 532.2 ± 6.0 Myr and 32.3 ± 0.7 Myr, respectively. Variable common Pb contents in the detrital
897 apatite unknowns were corrected by using a terrestrial Pb evolution model¹⁰⁴ for calculation of
898 single-grain ages followed by an iterative calculation to obtain single-analysis ^{207}Pb -corrected
899 ages¹⁰⁵. Alternatively, the range of $^{207}Pb_c / ^{206}Pb_c$ values for West Antarctic basement¹⁰⁶ can be
900 used for the single-grain age calculation: the resulting single-grain ages are within 1 Myr of the
901 single-grain ages obtained using the iterative calculation. Apatite U-Pb age filtering¹¹⁶
902 permitted grains with ages of 10–100 Myr to have 2σ errors $\leq 50\%$ and grains with ages > 100
903 Myr to have 2σ errors $\leq 25\%$. For apatite trace-element analysis, the Lolite Trace Elements DRS
904 was utilised. NIST612 glass and Madagascar apatite¹¹⁷ were employed as the primary and
905 secondary reference materials respectively, with ^{43}Ca as an internal elemental standard¹¹⁸.

906

907 **Code availability**

908 The standard model code of the ‘Community Earth System Models’ (COSMOS) version
909 COSMOS-landveg r2413 (2009) is available upon request from the ‘Max Planck Institute for
910 Meteorology’ in Hamburg (<https://www.mpimet.mpg.de>). G.L. and I.N. provide analytical
911 scripts upon request.

912

913 **Data availability**

914 All data are available online in the *Data Base for Earth and Environmental Science*
915 (PANGAEA)”. DOI registration in progress. The dataset can already be accessed via
916 <https://www.pangaea.de/tok/c29ccbd70a3a1dae9e4b4711c3b50cf25287a201>.

917

918 56. Stalling, D., Westerhoff, M. & Hege, H.-C. Amira: A Highly Interactive System for
919 Visual Data Analysis. *In: Hansen, C. D. and Johnson, C. R. (eds.) The Visualization*
920 *Handbook, Elsevier, The Netherlands, 749–767 (2005).*

- 921 57. Raine, J.I., Mildenhall, D.C. & Kennedy, E.M. New Zealand fossil spores and pollen:
922 an illustrated catalogue. 4th edition. *GNS Science miscellaneous series 4*,
923 <http://data.gns.cri.nz/sporepollen/index.htm>" (2011).
- 924 58. Mays, C. A late Cretaceous (Cenomanian-Turonian) south polar palynoflora from the
925 Chatham Islands, New Zealand. *Memoirs of the Association of Australasian*
926 *Palaeontologists* **47**, 92 pp (2015).
- 927 59. Bowman, V. C., Francis, J. E., Askin, R. A., Riding, J. B. & Swindles, G. T. Latest
928 Cretaceous-earliest Paleogene vegetation and climate change at the high southern
929 latitudes: palynological evidence from Seymour Island, Antarctic Peninsula.
930 *Palaeogeogr. Palaeoclimatol. Palaeoecol.* **408**, 26–47 (2014).
- 931 60. Utescher, T. et al. The Coexistence Approach—Theoretical background and practical
932 considerations of using plant fossils for climate quantification. *Palaeogeogr.*
933 *Palaeoclimatol. Palaeoecol.* **410**, 58–73 (2014).
- 934 61. Ballantyne, A.P., Greenwood, D.R., Sinninghe Damsté, J.S., Csank, A.Z., Eberle, J.J.
935 & Rybczynski, N. Significantly warmer Arctic surface temperatures during the
936 Pliocene indicated by multiple independent proxies. *Geology* **38**, 603–606 (2010).
- 937 62. Uhl, D., Mosbrugger, V., Bruch, A. & Utescher, T. Reconstructing palaeotemperatures
938 using leaf floras—case studies for a comparison of leaf margin analysis and the
939 coexistence approach. *Rev Palaeobot and Palynol* **126**, 49–64 (2003).
- 940 63. Pound, M.J. & Salzmann, U. Heterogeneity in global vegetation and terrestrial climate
941 change during the late Eocene to early Oligocene transition. *Scientific Reports* **7**,
942 43386 (2017).
- 943 64. Pross, J. et al. Persistent near-tropical warmth on the Antarctic continent during the
944 early Eocene epoch. *Nature* **488**, 73–77 (2012).
- 945 65. Willard, D. A. et al. Arctic vegetation, temperature, and hydrology during Early
946 Eocene transient global warming events. *Global and Planetary Change* **178**, 139–152
947 (2019).

- 948 66. Kennedy, E.M. Late Cretaceous and Paleocene terrestrial climates of New Zealand:
949 leaf fossil evidence from South Island assemblages. *N. Z. J. Geol. Geophys.* **46**, 295–
950 306 (2003).
- 951 67. Kennedy, E.M., Arens, N.C., Reichgelt, T., Spicer, R.A., Spicer, T.E.V., Stranks, L.,
952 Yang, J. Deriving temperature estimates from southern hemisphere leaves.
953 *Palaeogeogr. Palaeoclimatol. Palaeoecol.* **412**, 80–90 (2014).
- 954 68. Grimm, G. W., Bouchal, J. M., Denk, T. & Potts, A. Fables and foibles: A critical
955 analysis of the Palaeoflora database and the Coexistence Approach for
956 palaeoclimate reconstruction. *Rev. Palaeobot. Palynol.* **233**, 216–235 (2016).
- 957 69. Hollis, C. J. et al. The DeepMIP contribution to PMIP4: methodologies for selection,
958 compilation and analysis of latest Paleocene and early Eocene climate proxy data,
959 incorporating version 0.1 of the DeepMIP database. *Geosci. Model Dev.* **12**, 3149–
960 3206 (2019).
- 961 70. Kühl, N., Gebhardt, C., Litt, T. & Hense, A. Probability Density Functions as
962 Botanical-Climatological Transfer Functions for Climate Reconstruction. *Quat. Res.*
963 **58**, 381–392 (2002).
- 964 71. Greenwood, D.R., Keefe, R.L., Reichgelt, T. & Webb, J.A. Eocene paleobotanical
965 altimetry of Victoria's Eastern Uplands. *Australian Journal of Earth Sciences* **64**, 625–
966 637 (2017).
- 967 72. Harbert, R. S. & Nixon, K. C. Climate reconstruction analysis using coexistence
968 likelihood estimation (CRACLE): A method for the estimation of climate using
969 vegetation. *American Journal of Botany* **102**, 1277–1289 (2015).
- 970 73. GBIF. The Global Biodiversity Information Facility. What is GBIF?. Available from
971 <https://www.gbif.org/what-is-gbif> [15.5.2019] (2019).
- 972 74. Fick, S.E. & Hijmans, R.J. WorldClim 2: new 1-km spatial resolution climate surfaces
973 for global land areas. *Int. Journ. of Climatol.* **37**, 4302–4315 (2017).
- 974 75. Hijmans, R.J, Phillips, S., Leathwick, J. & Elith, J. Package 'dismo'. Available online
975 at: <http://cran.r-project.org/web/packages/dismo/index.html> (2011).

- 976 76. Reichgelt, T., West, C. K. & Greenwood, D. R. The relation between global palm
977 distribution and climate. *Scientific Reports* **8**, 4721 (2018).
- 978 77. Bourbonniere, R. A. & Meyers, P. A. Sedimentary geolipid records of historical changes
979 in the watersheds and productivities of Lakes Ontario and Erie. *Limnology and*
980 *Oceanography* **41**, 352–359 (1996).
- 981 78. Rütters, H. Sass, H., Cypionka, H. & Rullkötter, J. Phospholipid analysis as a toll to
982 study complex microbial communities in marine sediments. *J. Microbiol. Meth.* **48**,
983 149–160 (2002).
- 984 79. Bauersachs, T., Talbot, H. M., Sidgwick, F., Sivonen, K. & Schwark, L. Lipid
985 biomarker signatures as tracers for harmful cyanobacterial blooms in the Baltic Sea.
986 *PLOS ONE* **12**, doi:10.1371/journal.pone.0186360 (2017).
- 987 80. Bauersachs, T., et al. Rapid analysis of long-chain glycolipids in heterocystous
988 cyanobacteria using high-performance liquid chromatography coupled to electrospray
989 ionization tandem mass spectrometry. *Rapid Comm. in Mass Spectrometry* **23**, 1387–
990 1394 (2009).
- 991 81. Bauersachs, T., et al. Distribution of long chain heterocyst glycolipids in cultures of
992 the thermophilic cyanobacterium *Mastigocladus laminosus* and a hot spring microbial
993 mat. *Org. Geochem.* **56**, 19 – 24 (2013).
- 994 82. Wörmer, L., et al. Cyanobacterial heterocyst glycolipids in cultures and environmental
995 samples: Diversity and biomarker potential. *Limnol. Oceanogr.* **57**, 1775–1788
996 (2012).
- 997 83. Schouten, S., et al. Endosymbiotic heterocystous cyanobacteria synthesize different
998 heterocyst glycolipids than free-living heterocyst cyanobacteria. *Phytochemistry* **85**,
999 115–121 (2013).
- 1000 84. Bale, N. J., et al. A novel heterocyst glycolipid detected in a pelagic N₂-fixing
1001 cyanobacterium of the genus *Calothrix*. *Org. Geochem.* **123**, 44–47 (2018).

- 1002 85. Bauersachs, T., Miller, S. R., Gugger, M., Mudimu, O., Friedl, T. & Schwark, L.
1003 Heterocyte glycolipids indicate polyphyly of stigonematalean cyanobacteria.
1004 *Phytochem.* **166**, doi:10.1016/j.phytochem.2019.112059 (2019).
- 1005 86. Ehrmann, W. et al. Provenance changes between recent and glacial-time sediments in
1006 the Amundsen Sea Embayment, West Antarctica: clay mineral assemblage evidence.
1007 *Antarctic Science* **23**, 471–486 (2011).
- 1008 87. Petschick, R., Kuhn, G. & Gingele, F. Clay mineral distribution in surface sediments
1009 of the South Atlantic: sources, transport, and relation to oceanography. *Mar. Geol.*
1010 **130**, 203–229 (1996).
- 1011 88. Kirschvink, J. L. The least-squares line and plane and the analysis of paleomagnetic
1012 data. *J. Royal Astr. Soc.* **62**, 699–718 (1980).
- 1013 89. Roeckner, E., et al. The atmospheric general circulation model ECHAM 5. In: PARTI:
1014 Model Description, Report 349, Max-Planck-Institut für Meteorologie, Hamburg (2003).
- 1015 90. Marsland, S.J., Haak, H., Jungclaus, J.H., Latif, M. & Roske, F. The Max-Planck-
1016 Institute global ocean/sea ice model with orthogonal curvilinear coordinates. *Ocean*
1017 *Model* **5**, 91–127 (2003).
- 1018 91. Hagemann, S. & Dumenil, L. A parametrization of the lateral waterflow for the global
1019 scale. *Clim. Dyn.* **14**, 17–31 (1997).
- 1020 92. Hibler III, W.D. A dynamic thermodynamic sea ice model. *J. Phys. Oceanogr.* **9**, 815–
1021 846 (1979).
- 1022 93. Markwick, P.J. & Valdes, P.J. Palaeo-digital elevation models for use as boundary
1023 conditions in coupled ocean–atmosphere GCM experiments: a Maastrichtian (late
1024 Cretaceous) example. *Palaeogeogr. Palaeoclimatol. Palaeoecol.* **213**, 37–63 (2004).
- 1025 94. Sewall, J.O., Van de Wal, R.S.W., Van Der Zwan, K., Van Oosterhout, C., Dijkstra,
1026 H.A. & Scotese, C.R. Climate model boundary conditions for four Cretaceous time
1027 slices. *Clim. Past* **3**, 647–657 (2007).

- 1028 95. Niezgodzki, I., Tyszka, J., Knorr, G., & Lohmann, G. Was the Arctic Ocean ice free
1029 during the latest Cretaceous? The role of CO₂ and gateway configurations. *Global*
1030 *and Planetary Change* **177**, 201–212 (2019).
- 1031 96. Wei, W. & Lohmann, G. Simulated Atlantic Multidecadal Oscillation during the
1032 Holocene. *J. Climate* **25**, 6989–7002 (2012).
- 1033 97. Zhang, X., Lohmann, G., Knorr, G., & Purcell, C. Abrupt glacial climate shifts
1034 controlled by ice sheet changes. *Nature* **512**, 290–294 (2014).
- 1035 98. Stepanek, C. & Lohmann, G. Modelling mid-Pliocene climate with COSMOS.
1036 *Geosci. Model Dev.* **5**, 1221–1243 (2012).
- 1037 99. Knorr, G. & Lohmann, G. Climate warming during Antarctic ice sheet expansion at
1038 the Middle Miocene transition. *Nat. Geosci.* **7**, 376–381 (2014).
- 1039 100. Stein, R. *et al.* Evidence for ice-free summers in the late Miocene central
1040 Arctic Ocean. *Nat. Comm.* **7**, 11148 (2016).
- 1041 101. Walliser, E.O., Lohmann, G., Niezgodzki, I., Tütken, T. & Schöne, B.R.
1042 Response of Central European SST to atmospheric pCO₂ forcing during the
1043 Oligocene – A combined proxy data and numerical climate model approach.
1044 *Palaeogeogr. Palaeoclimatol. Palaeoecol.* **459**, 552–569 (2016).
- 1045 102. Vahlenkamp, M., *et al.* Astronomically Paced Changes in Deep-Water
1046 Circulation in the Western North Atlantic during the Middle Eocene. *Earth Planet. Sci.*
1047 *Lett.* **484**, 329–340 (2018).
- 1048 103. Gierz, P., Lohmann, G. & Wei, W. Response of Atlantic Overturning to Future
1049 Warming in a coupled Atmosphere-Ocean-Ice Sheet Model. *Geophys. Res. Lett.* **42**,
1050 6811–6818 (2015).
- 1051 104. Simões Pereira, P., van de Flierdt, T., Hemming, S.R., Hammond, S.J., Kuhn,
1052 G., Brachfeld, S., Doherty, C. & Hillenbrand, C.D. Geochemical fingerprints of
1053 glacially eroded bedrock from West Antarctica: Detrital thermochronology, radiogenic
1054 isotope systematics and trace element geochemistry in Late Holocene glacial-marine
1055 sediments. *Earth-Science Rev.* **182**, 204–232 (2018).

- 1056 105. Stacey, J. S. & Kramers, J.D. Approximation of terrestrial lead isotope
1057 evolution by a two-stage model. *Earth Planet. Sci. Lett.* **26**, 207–221 (1975).
- 1058 106. Chew, D. M., Sylvester, P. J. & Tubrett, M. N. U–Pb and Th–Pb dating of
1059 apatite by LA-ICPMS. *Chem. Geol.* **280**, 200–216 (2011).
- 1060 107. O’Sullivan, G. J., Chew, D. M., Morton, A. C., Mark, C. & Henrichs, I. A. An
1061 Integrated Apatite Geochronology and Geochemistry Tool for Sedimentary
1062 Provenance Analysis. *Geochem. Geophys. Geosys.* **19**, 1309–1326 (2018).
- 1063 108. Flowerdew, M.J., Tyrrell, S., Riley, T.R., Whitehouse, M.J., Mulvaney, R., Leat,
1064 P.T. & Marschall, H.R. Distinguishing East and West Antarctic sediment sources using
1065 the Pb isotope composition of detrital K-feldspar. *Chem. Geol.* **292–293**, 88–102
1066 (2012).
- 1067 109. Petrus, J. A., & Kamber, B. S. VizualAge: A novel approach to laser ablation
1068 ICP-MS U-Pb geochronology data reduction. *Geostandards and Geoanalytical
1069 Research* **36**, 247–270 (2012).
- 1070 110. Chew, D.M., Petrus, J. A. & Kamber, B. S. U-Pb LA-ICPMS dating using
1071 accessory mineral standards with variable common Pb. *Chem. Geol.* **363**, 185–199
1072 (2014).
- 1073 111. C. Paton, Hellstrom, J., Paul, B.; Woodhead, J., Hergt, J. Lolite: freeware for
1074 the visualisation and processing of mass spectrometric data. *J. Anal. At.
1075 Spectrom.* **26**, 2508–2518 (2011).
- 1076 112. Ludwig, K. R. User’s manual for Isoplot 3.75: A geochronological Toolkit for
1077 Microsoft Excel. *Berkeley Geochronology Center Special Publication* **4**, 70 (2012).
- 1078 113. Nasdala, L. et al. GZ7 and GZ8 - Two Zircon Reference Materials for SIMS U-
1079 Pb Geochronology. *Geostandards and Geoanalytical Research* **42**, 431–457 (2018).
- 1080 114. McDowell, F. W., McIntosh, W. C. & Farley, K. A. A precise ^{40}Ar – ^{39}Ar
1081 reference age for the Durango apatite (U–Th)/He and fission-track dating standard.
1082 *Chem. Geol.* **214**, 249–263 (2005).

- 1083 115. Schoene, B. & Bowring, S. A. U–Pb systematics of the McClure Mountain
 1084 syenite: thermochronological constraints on the age of the 40 Ar/39 Ar standard
 1085 MMhb. *Contributions to Mineralogy and Petrology* **151**, 615 (2006).
- 1086 116. Mark, C., Cogné, N. & Chew, D. Tracking exhumation and drainage divide
 1087 migration of the western Alps: a test of the apatite U-Pb thermochronometer as a
 1088 detrital provenance tool. *GSA Bulletin* **128**, 1439–1460 (2016).
- 1089 117. Mao, M., Rukhlov, A.S., Rowins, S.M., Spence, J. & Coogan, L.A. Apatite
 1090 trace element compositions: A robust new tool for mineral exploration. *Econom. Geol.*
 1091 **111**, 1187–1222 (2016).
- 1092 118. Woodhead, J.D., Hellstrom, J., Hergt, J.M., Greig, A. & Maas, R. Isotopic and
 1093 elemental imaging of geological materials by laser ablation inductively coupled
 1094 plasma-mass spectrometry. *Geostandards and Geoanalytical Research* **31**, 331–343
 1095 (2007).

1096

1097 Extended Data Figure 1: Tera-Wasserburg and PCA plots for U/Pb ages. a) Tera-
 1098 Wasserburg diagram showing apatite (red; 9.9 mbsf) and zircon (blue; 26.7 mbsf) U-Pb data.
 1099 Red bar at upper array intercept for Eocene apatite is the range of crystalline basement
 1100 $^{207}\text{Pb}/^{206}\text{Pb}_c$ values reported by (ref. 105) for West Antarctica, which anchor the apatite age
 1101 calculation. Data-point error ellipses are 2σ . b) PCA plot showing trace-element data and
 1102 single-grain ages for AWI-35 (9.9 mbsf) apatite, and lithological fields derived from bedrock
 1103 apatite reference library¹⁰⁵. Eocene grains (labelled in red) are chemically as well as
 1104 chronologically distinct from other detrital apatite in the same sample. Data-point error
 1105 ellipses are 2σ .

1106

1107 Extended Data Figure 2: Pollen abundance diagram. Percentages of most abundant pollen
 1108 and spores and their total counts in cores 9R and 10R at site PS104_20-2.

1109

1110 Extended Data Figure 3: Photomicrographs of selected pollen and spores. a. *Cyathidites*
1111 *australis*; b. *Osmundacidites wellmanii*; c. *Ruffordiaspora australiensis*; d. *Ruffordiaspora*
1112 *ludbrookiae*; e. *Cycadopites follicularis*; f. *Microcachrydites antarcticus*; g. *Phyllocladidites*
1113 *mawsonii*; h. *Podocarpidites major*; i. *Trichotomosulcites hemisphaerius*; j.
1114 *Trichotomosulcites subgranulatus*; k. *Taxodiaceapollenites hiatus*; l. *Equisetosporites sp.*;
1115 m. *Nyssapollenites chathamicus*; n. *Peninsulapollis gillii*; o. *Proteacidites subpalisadus*. All
1116 scale bars: 10 μ m.

1117
1118 Extended Data Figure 4: Heterocyst glycolipid palaeothermometry. Presence of heterocyst
1119 glycolipids at 27.03–27.04 mbsf at site PS104_20-2 (core 9R) and river or lake surface water
1120 temperature (SWT) estimates from the heterocyst glycolipid-based molecular
1121 palaeothermometer.

1122
1123 Extended Data Figure 5: Example of microscopic images from thin sections. The sections
1124 are taken from a fossil root fragment between 29.34 and 29.43 mbsf in core 10R at site
1125 PS104_20-2. a) Overview scan of root fragment with indicated locations of detailed
1126 microscopic images b–e. White arrows indicate locations of preserved parenchyma storage
1127 cells including potential aerenchyma gas exchange cells (d). The scale bar in “d” applies to
1128 figures b–e.

1129
1130 Extended Data Figure 6: Biomarker presence. a) Pristane/*n*-C₁₇ versus phytane/*n*-C₁₈ to infer
1131 organic matter type during sediment deposition (after refs. 39, 40). b) Carbon preference
1132 index (CPI) and pristane/phytane (Pr/Ph) ratios. The CPI points to a low maturity and land
1133 plant origin of the organic matter (CPI > 1) deposited in an aquatic environment (Pr/Ph <2)
1134 and a peat swamp environment (Pr/Ph >2), respectively.

1135
1136 Extended Data Table 1: Percentages of most abundant pollen and spore taxa.

1137

1138 Extended Data Table 2: Selected key pollen taxa and NLR used to derive quantitative
1139 climate estimates.

1140

1141 Extended Data Table 3: Full list of identified pollen and spore taxa. All taxa identified
1142 during the current study are included. Question marks show uncertain taxa
1143 identifications, which require further studies. Those taxa marked with an asterisk
1144 have also been described from the Tupurangi Formation on the Chatham Islands^{30,58}.